

# XMAGNET: Velocity structure functions of AGN-driven turbulence in the multiphase intracluster medium

M. Fournier<sup>1</sup>, P. Grete<sup>1</sup>, M. Brüggen<sup>1</sup>, B. W. O’Shea<sup>2,3,4,5</sup>, D. Prasad<sup>6</sup>,  
B. D. Wibking<sup>3</sup>, F. W. Glines<sup>7</sup>, R. Mohapatra<sup>8</sup>

<sup>1</sup> Universität Hamburg, Hamburger Sternwarte, Gojenbergsweg 112, 21029 Hamburg, Germany  
e-mail: martin.fournier@uni-hamburg.de

<sup>2</sup> Department of Computational Mathematics, Science, and Engineering, Michigan State University, East Lansing, MI 48824, USA

<sup>3</sup> Department of Physics and Astronomy, Michigan State University, East Lansing, MI 48824, USA

<sup>4</sup> Facility for Rare Isotope Beams, Michigan State University, East Lansing, MI 48824, USA

<sup>5</sup> Institute for Cyber-Enabled Research, 567 Wilson Road, Michigan State University, East Lansing, MI 48824

<sup>6</sup> School of Physics and Astronomy, Cardiff University, 5 The Parade, Cardiff CF24 3AA, UK

<sup>7</sup> Theoretical Division, TA-3 Bldg. 123, Los Alamos National Laboratory, Los Alamos, NM 87545

<sup>8</sup> Department of Astrophysical Sciences, Princeton University, NJ 08544, USA

Received February 28, 2025

## ABSTRACT

*Context.* Significant theoretical and observational efforts are underway to investigate the properties of turbulence in the hot plasma that pervades galaxy clusters. Spectroscopy has been used to study the projected line-of-sight velocities in both the hot intracluster medium and the cold gas phase using optical and X-ray telescopes.

*Aims.* We characterize the velocity structure functions (VSFs) of the multiphase intracluster medium in a simulated galaxy cluster core and study the effects of projections on the hot and cold phase of the gas.

*Methods.* We use the fiducial run of the XMAGNET suite, a collection of exascale magneto-hydrodynamical simulations of a cool-core cluster, to compute velocity structure functions. The simulation includes radiative cooling as well as a model for active galactic nuclei feedback.

*Results.* Examining three-dimensional and line-of-sight velocity structure functions, we find no clear correlation between the behavior of the hot ( $10^6 \text{ K} \leq T \leq 10^8 \text{ K}$ ) and cold ( $T \leq 10^5 \text{ K}$ ) phases VSFs. Assuming a power law model for the VSF, we find that the power law index  $m$  of the cold phase varies significantly throughout the 4 Gyr simulation time. We compare our VSFs with observations using mock optical and X-ray images, and conclude that projection effects significantly impact the amplitude and power law index of both the hot and cold phases. In the cold phase, applying a Gaussian smoothing filter to model effects of atmospheric seeing increases significantly the power law index of the projected VSF at scales below the filter’s kernel size. Moreover, the VSF amplitude and power law index vary significantly depending on the viewing orientation.

*Conclusions.* Observational biases such as projection effects, atmospheric seeing and the viewing angle cannot be ignored when interpreting line-of-sight velocity structure of the intracluster medium.

**Key words.** galaxies: clusters: intracluster medium – galaxies: jets – galaxies: clusters: general – methods: numerical – magnetohydrodynamics

## 1. Introduction

Around 10% of the total mass of galaxy clusters is thought to be contained in a hot plasma of ionized gas, usually designated as the intracluster medium (ICM) (e.g., Chiu et al. 2015). Cooling via Bremsstrahlung gives rise to the emission of radiations, making clusters strong X-ray sources (Felten et al. 1966; Mitchell et al. 1976; Serlemitsos et al. 1977; Sarazin 1986). Mass estimates of clusters, as well as density or temperature profiles, can be derived from observations of this emission assuming that the ICM is in hydrostatic equilibrium. However, both simulations and observations have shown that several processes are likely to cause deviations to the hydrostatic equilibrium (Rasia et al. 2006; Lau et al. 2013; Biffi et al. 2016; Barnes et al. 2021). In particular, it is expected that non-thermal sources of pressure, such as turbulence, might add to the thermal pressure support of the ICM against gravity (Fusco-Femiano & Lapi 2017; Angelinelli et al. 2020; Vazza et al. 2011).

Cluster mergers are thought to be the main drivers of turbulence on the scale of entire clusters. In a typical merger event, two clusters collide with relative velocities of  $\sim 10^3 \text{ km s}^{-1}$ . As the ICM relaxes in the post-merger phase, shocks form and propagate through the ICM, carrying an energy of up to  $10^{65} \text{ erg}$  and providing heat to the plasma on scales of  $\sim \text{Mpc}$  (e.g., Markevitch & Vikhlinin 2007). The subsequent dissipation of turbulence heats the ICM on longer time scales. Results from hydrodynamical simulations suggest that turbulent kinetic energy in perturbed clusters resulting from mergers can account for up to 20 – 30 % of the ICM’s thermal energy (Dolag et al. 2005; Vazza et al. 2011). A common consequence of mergers in galaxy clusters is a temporary offset of the gas core with respects to its dark matter counterparts. In such cases, the ICM falls back towards the center of the cluster and forms a spiral pattern that can drive turbulence on scales of up to 100 kpc (ZuHone et al. 2013). In the innermost regions of galaxy clusters, active galactic nuclei (AGN) are suspected to be the main drivers of turbulence (Scan-

napieco & Brügger 2008; Li et al. 2020). By accelerating jets of gas up to relativistic speeds, AGN inflate cavities in the ICM which rise buoyantly and propagate out to distances of a few kpc to hundreds of kpc (Bîrzan et al. 2004; Dunn et al. 2005; Prunier et al. 2024). As they rise, these cavities displace the ICM, mix with the surrounding gas and inject turbulent energy (Brügger et al. 2009; Gatuzz et al. 2024).

Constraining turbulence with observations is challenging and typically relies on indirect measurements. X-ray surface brightness (SB) fluctuations can be computed by subtracting smoothed models from the SB data (Churazov et al. 2012; Zhuravleva et al. 2014). The velocity power spectrum of the gas can then be inferred from the power spectrum of the SB fluctuations, subject to a range of assumptions. X-ray calorimeters can also provide measurements of the typical turbulent velocities in cluster cores through line broadening measurements (Hitomi Collaboration et al. 2016; XRISM Collaboration 2025). More recently, Li et al. (2020) have proposed to use observations of ionized filaments found in the inner tens of kpc of cool-core clusters to probe the turbulent motion of the ICM. Such filamentary structures are common in cool-core clusters (Olivares et al. 2019), and are thought to originate from thermal instabilities in the ICM (McCourt et al. 2012), likely seeded by AGN outflows (Li & Bryan 2014; Fournier et al. 2024). The line-of-sight velocity of these filaments can be obtained from optical spectrometers with angular resolutions of less than  $\sim 10^{-1}$  arcsec<sup>2</sup>. By measuring the velocity structure function (VSF) of the filaments, Li et al. (2020) found deviations from a Kolmogorov scaling characterized by a steeper power law index than the expected  $\ell^{1/3}$ , where  $\ell$  designates the spatial scale. The origin of this steepening is subject to debate in the literature. One hypothesis is that it is related to the injection of turbulence caused by the AGN. As the bubbles rise in the ICM, they could drive turbulence and increase the amplitude of the VSF at scales of the order of their typical size (i.e.,  $\sim 10$  kpc). Other possibilities include the contribution of gravitational acceleration (Wang et al. 2021), or the condensation of cold gas within supersonic outflows (Hu et al. 2022), which have both been found to result in VSFs steeper than the Kolmogorov scaling law. The interpretation of these observations could be affected by projection effects or limited angular resolution. Some of these effects have been investigated in turbulent box simulations (Mohapatra et al. 2022) and idealized cluster setups (ZuHone et al. 2016; Wang et al. 2021; Sotira et al. 2024).

In this paper, we use a high-resolution exascale MHD simulation from the XMAGNET project<sup>1</sup> to characterize the VSFs of the multi-phase ICM. We explore the effects of projection, emission weighting, atmospheric seeing and viewing angle on the VSF. In Sect. 2, we describe our numerical method and our simulation parameters. In Sect. 3, we quantify the turbulent motions of both the hot and cold phases using first order VSF. In Sect. 4, we investigate up to what extent projection effects might affect the measurement of the VSF, before discussing these results in Sect. 5 and concluding in Sect. 6.

## 2. Method

### 2.1. Simulation suite and initial conditions

The XMAGNET simulation suite used in this study is introduced and described in Grete et al. (subm.). Hereafter, we summarize the key points of the methodology presented in that paper.

<sup>1</sup> See <https://xmagnet-simulations.github.io/> for an overview.

We ran hydrodynamical and MHD simulations of an idealised cool-core cluster on the Frontier supercomputer<sup>2</sup>. We used ATHENAPK<sup>3</sup>, a performance-portable version of the ATHENA++ astrophysical magnetohydrodynamics code (Stone et al. 2020). It is based on the block-structured refinement framework PARTHENON (Grete et al. 2023a) and includes magnetic fields, radiative cooling, and AGN and stellar feedback. The simulations used an overall second-order accurate, shock-capturing, finite-volume scheme consisting of RK2 time integration, piecewise-linear reconstruction, and an HLLD Riemann solver (Miyoshi & Kusano 2005).

Gravity is treated as an acceleration term parametrised by a superposition of a Navarro-Frenk-White (NFW) profile (Navarro et al. 1997), a Hernquist potential representing the brightest central galaxy’s mass (Hernquist 1990), and a central point mass modelling the effect of 3C 84, the supermassive black hole (SMBH) in the Perseus cluster’s BCG. The initial gas distribution is calculated numerically to obey hydrostatic equilibrium assuming the entropy profile of the Perseus cluster from the ACEPT catalogue (Cavagnolo et al. 2009). Optically thin cooling is calculated by the exact integration method introduced by Townsend (2009) and uses solar metallicity cooling tables by Schure et al. (2009). Velocity and magnetic perturbations are seeded at  $t = 0$  to break the symmetry of the system, with respective dispersion of  $\delta v = 75$  km s<sup>-1</sup> and  $\delta B = 1$   $\mu$ G. These perturbations are generated using an inverse parabolic spectrum with a peak scale of 100 kpc. AGN feedback is modelled via source terms for thermal, kinetic and magnetic energy. Cold material (defined as gas of temperature  $T \leq 10^5$  K) is accreted at a rate  $\dot{M}_{\text{acc}}$  related to the accretion power by  $\dot{E}_{\text{acc}} = \eta \dot{M}_{\text{acc}} c^2$ , where  $\eta = 0.001$  is the accretion efficiency and  $c$  the speed of light. This accretion power is then split into the three feedback channels by their corresponding feedback fractions  $f_i$ , where  $i$  designates the kinetic, thermal and magnetic feedback channels. In the absence of star particles, stellar feedback is calculated analytically, by extracting gas denser than a density threshold  $n_{\text{thresh},*} = 50$  cm<sup>-3</sup> and redistributing it into thermal energy with an efficiency of  $5 \times 10^{-6}$ . The structure of the grid is identical in all our runs and kept constant across time. The root mesh grid is made of  $1,024^3$  cells covering a total volume of  $(6.4 \text{ Mpc})^3$ . The root grid is refined a further  $\ell_{\text{max}} = 6$  cubic and nested refinement levels. As a result, the maximally refined region has a volume of  $(250 \text{ kpc})^3$  and is covered by  $2,560^3$  cells of size  $\Delta_x = 97.7$  pc. The entire analysis presented in this paper is based on data extracted from this maximally refined region, i.e. for gas cells located at radii  $r \leq 125$  kpc.

In this study, we analyze the data from the fiducial simulation of the XMAGNET suite, i.e., the MHD run with solar metallicity cooling. The simulation is run for a total duration of 4 Gyr. A visualization of the inner 80 kpc at  $t = 3.2$  Gyr is presented in Fig. 1. It shows a projected map of the cold gas line-of-sight velocity, weighted by H $\alpha$  emission, overlaid on top of a projected temperature map of the hot ICM. A zoom on the innermost region shows a comparison between the original projection, and a smoothed version produced to mimic the effects of atmospheric seeing.

<sup>2</sup> Frontier is operated by the Oak Ridge National Laboratory’s Leadership Computing Facility on behalf of the Department of Energy. This work is supported by the DOE INCITE program under allocation AST-146 (2023-2024).

<sup>3</sup> ATHENAPK is available at <https://github.com/parthenon-hpc-lab/athenapk> and commit 3ce0a88 was used for the simulations.

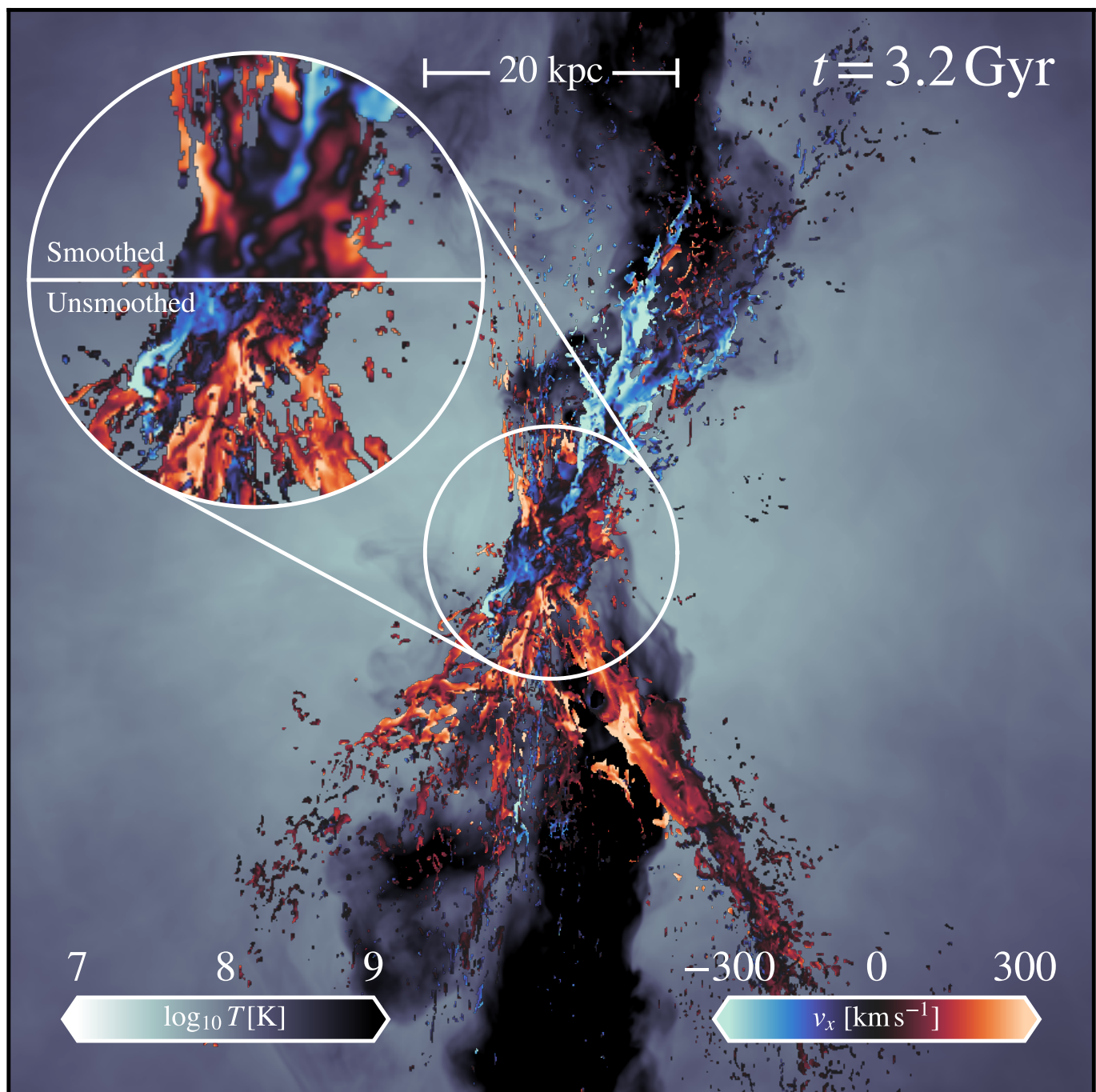


**Fig. 1.**  $H\alpha$  emission –weighted projection of the line-of-sight velocity for the inner 80 kpc of our simulated box, at  $t = 3.2$  Gyr. A zoom on the innermost region showcase the effect of atmospheric seeing on the map. The background image is a projection of the temperature field. The figure can be compared to Fig. 2 from [Li et al. \(2020\)](#).

## 2.2. Velocity structure functions

A useful tool to quantify the scaling of turbulence is the  $p$ th-order VSF. It is a two-point correlation function defined as:

$$S_p(\ell) = \langle |\mathbf{u}(\mathbf{x} + \ell \cdot \mathbf{e}) - \mathbf{u}(\mathbf{x})|^p \rangle, \quad (1)$$

where  $\mathbf{u}$  is the velocity field evaluated at a pair of points of positions  $\mathbf{x}$  and  $\mathbf{x} + \ell \cdot \mathbf{e}$ , and  $\mathbf{e}$  is a randomly oriented unit vector. It is expected that the VSF scales as  $S_p(\ell) \propto \ell^{p/3}$  in the inertial range, assuming that the turbulence is isotropic, homogeneous

and that the fluid is incompressible ([Kolmogorov 1941](#)). To facilitate direct comparison with observations, we will focus on the first-order VSFs (i.e.,  $S_1(\ell)$ ). It is worth noting that expressing the second order VSF  $S_2(\ell)$  in spectral space leads to the regular Kolmogorov scaling law:

$$E(k) \propto \varepsilon^{2/3} k^{-5/3}, \quad (2)$$

where  $E(k)$  is the turbulent energy spectrum,  $\varepsilon$  is the turbulent dissipation rate, and  $k$  the wavenumber. In [Appendix C](#), we also present second-order VSFs for comparison.

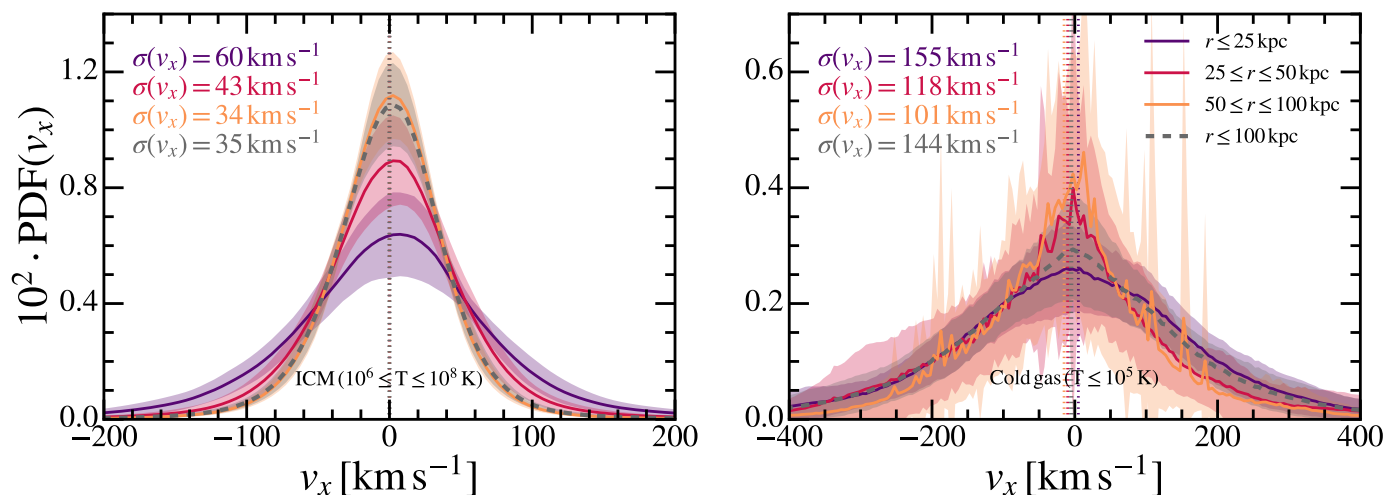


**Fig. 2.** PDF of the velocities'  $x$ -component for the hot phase ( $10^6 \leq T \leq 10^8$  K, left panel) and cold phase ( $T \leq 10^5$  K, right panel) for various radius bins and the PDF of all gas located at radii  $r \leq 100$  kpc. Vertical dashed lines indicate the median values. Colored areas represent the standard deviation resulting from time variation. We have verified that the  $y$ -component leads to similar results.

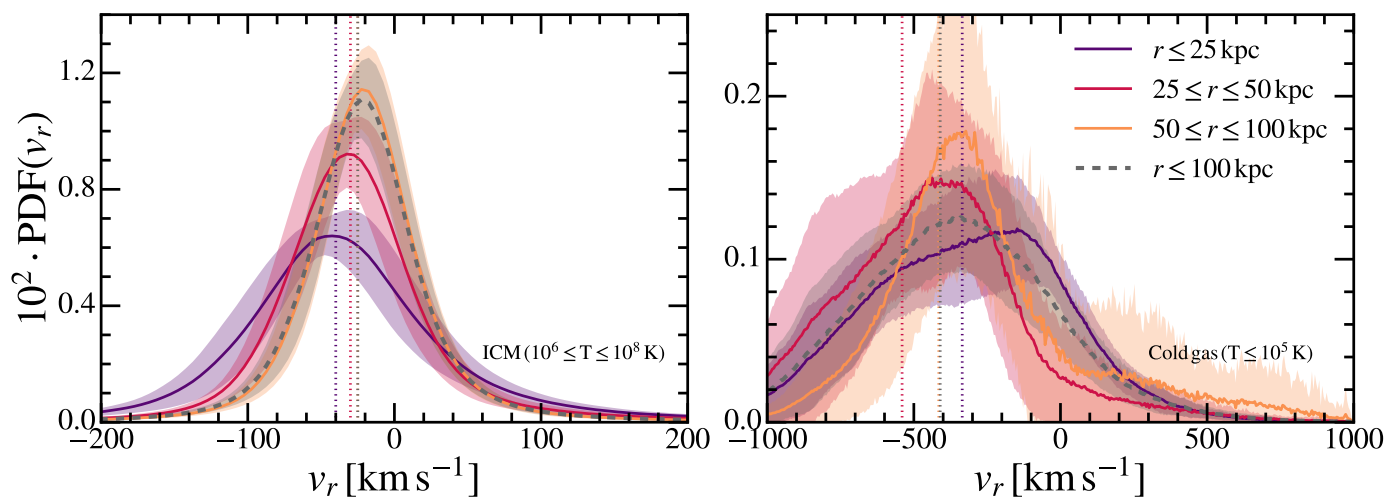


**Fig. 3.** Similar to Fig. 2 for radial velocity  $v_r$ .

We compute the VSF by randomly picking pairs of points separated by a distance  $\ell$ , calculate their associated velocity difference, and then average them into bins of logarithmically increasing size. Since we compute the VSFs in a region containing a relatively large number of cells (i.e.,  $1,024^3$ ), we employ a parallelized algorithm adapted from Federrath et al. (2010). Sampling pairs of points with separations of the order of a few cell sizes can be inefficient. When randomly selecting two cells in the grid, the probability of choosing a pair with separation  $\ell$  is proportional to  $\ell^2$ . Moreover, since the grid is discretized, the set of possible separations is not continuous. For separations smaller than 500 pc, we adjust the bin sizes to account for the discrete nature of the grid. Specifically, the separation between two cells is given by

$$\ell = \sqrt{i^2 + j^2 + k^2} \Delta_x, \quad (3)$$

where  $\Delta_x$  is the cell size and  $i, j, k$  are integers representing the displacement between the two cells along the three Cartesian directions of the grid. When the grid is two-dimensional (for instance when computing projected VSFs), Eq. 3 reduces

to  $\ell = \sqrt{i^2 + j^2} \Delta_x$ . In order to increase the efficiency of the point sampling, we randomly sampled  $N$  points on the grid, representing the first pixel of each pair. We then randomly sample a neighboring cell for each of these points following a uniform probability distribution of distance, up to 500 pc. The VSF above 500 pc is computed using a naive sampling of points (i.e., by uniformly sampling both pixels of each pair). The value of 500 pc has been chosen to maximize the efficiency of the code. We have verified that our results are equivalent to the VSF obtained when entirely computed from naive pair sampling. For projected VSF of the cold phase (see Sect. 4), the limited number of pixels allows us to calculate explicitly the velocity difference of all possible pairs of pixels. Convergence tests of our VSF algorithms are presented in the Appendix B.

### 3. Quantifying turbulence in the intracluster medium

#### 3.1. Velocity dispersion

The velocity distribution of the hot and cold gas averaged between 0.9 and 4 Gyr is presented in Fig. 2. Darker to brighter col-

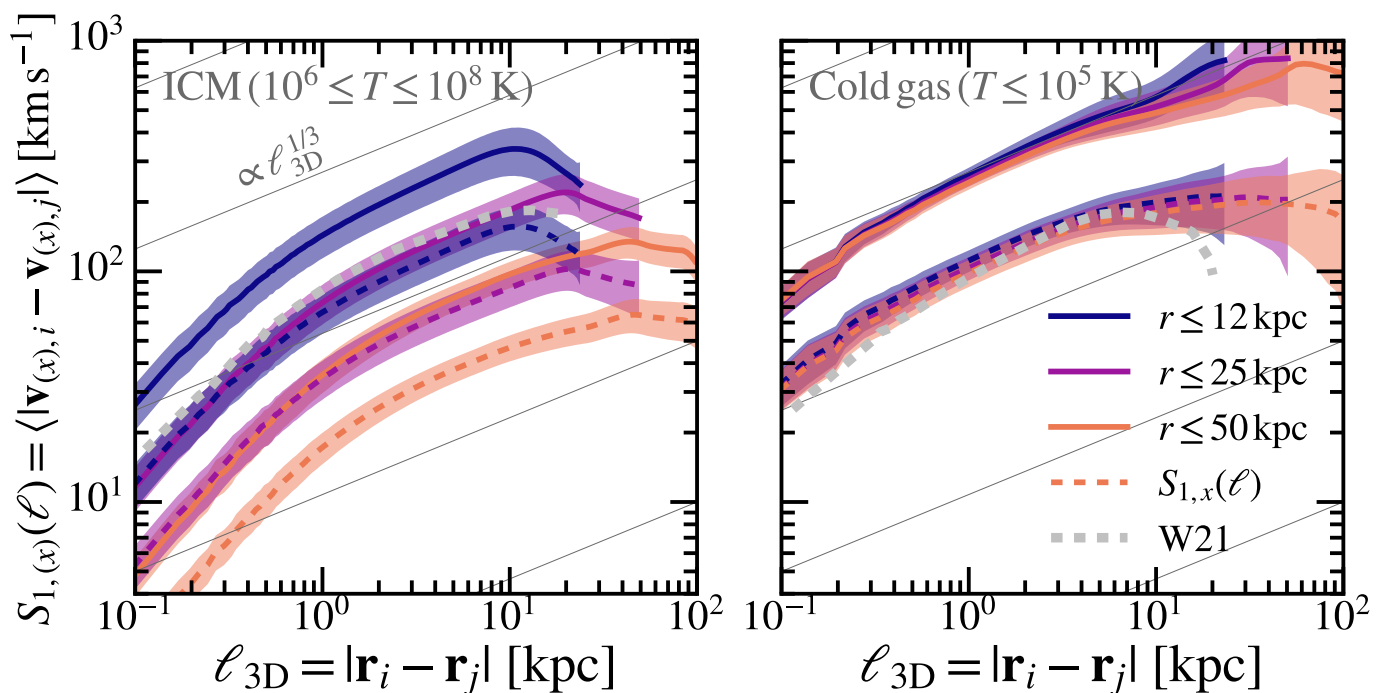


**Fig. 4.** VSF of the hot ICM (left panel) and the cold phase (right panel) for all gas located less than 12, 25 and 50 kpc away from the center of the simulated box. The dashed colored lines indicate the line-of-sight VSFs taking the  $x$ -component of the velocity field. We emphasize that the latter are not equivalent to projected VSFs, as the distance between pairs of cells is still three-dimensional (projected VSFs are discussed in Sect. 4). Colored area is showing standard deviation over time. The solid gray lines in the background indicate the Kolmogorov scaling law (Kolmogorov 1941). As our setup closely resembles the fiducial MHD run from Wang et al. (2021), we present the time-averaged line-of-sight VSFs for the hot and cold phases from that work, for radii  $r \lesssim 10$  kpc (dashed grey line labeled W21). A comparison of our results with this study is discussed in Sect. 5.2. We emphasize that VSFs below separations of  $\ell \sim 800$  pc are likely to be steepened by the effect of numerical viscosity.

ored curves represent annuli with increasing distances from the center, namely  $r \leq 25$  kpc,  $25 \leq r \leq 50$  kpc and  $50 \leq r \leq 100$  kpc. The dashed gray curves indicate the data for the gas located at radii  $r \leq 100$  kpc. The standard deviation  $\sigma(v_x)$  for each curve is derived by fitting a Gaussian function to each distribution. The colored areas represent the standard deviation resulting from time variation. The colored dashed lines indicate the median velocity. The standard deviation of the velocity of the hot gas decreases with increasing radius by roughly a factor of two between the inner and the outer regions of the maximally refined region of our simulated box, with a value of  $\sim 60$  km s $^{-1}$  in the innermost region. This value is relatively low compared to measurements of X-ray calorimeters (Hitomi Collaboration et al. 2016), but consistent with other idealized setups similar to ours (Wang et al. 2021; Ehlert et al. 2021). This could indicate that the contribution of other sources of turbulence, such as mergers, sloshing, or accretion cannot be ignored to reproduce the measured velocity dispersions. The velocity distribution of the cold phase is much wider, with dispersions of the order of  $\sim 150$  km s $^{-1}$  in the innermost region. We have verified that including emission-weighting does not significantly impact these results.

### 3.2. Radial velocity

Similarly, we present the distribution of the radial velocity of the hot and cold gas in Fig. 3. The hot phase (left panel) distribution is characterized by a negative mean radial velocity, as large as  $\sim -50$  km s $^{-1}$  in the innermost region and  $\sim -20$  km s $^{-1}$  when including the whole maximally refined region. The velocity distribution of the cold phase is more complex and radially depen-

dent. In the outermost region, it follows a broadly Gaussian distribution with a mean radial velocity of  $\sim -400$  km s $^{-1}$ . In the innermost region, the distribution is broader and more asymmetric. At the lower end of the distribution the velocity goes down to  $\sim -10^3$  km s $^{-1}$ . A higher tail of positive radial velocity is also visible and is likely related to uplifting of warm and cold gas resulting from the coupling with the outflowing jets (see also Fournier et al. 2024). Overall, the motions of the hot and cold phases are mostly decoupled. The cold phase is dominated by a ballistically infalling motion, while the hot phase only slightly deviates from hydrostatic equilibrium.

### 3.3. Velocity structure functions

#### 3.3.1. Overall intracluster medium velocity structure functions

In Fig. 4, we present the three-dimensional VSF (i.e., obtained taking the three-dimensional distance between pairs of cells) of the hot (left panel) and cold (right panel) phases. The solid (dashed) lines indicate the VSFs obtained from the magnitude of the three-dimensional velocity vectors ( $x$ -component of the velocity vectors) of each pairs of cells, respectively. Shaded areas indicate time variation throughout the whole active part of the simulation (i.e., starting from the formation of the first cold structures at  $t \sim 0.9$  Gyr). The different colors indicate VSFs obtained including gas located from various radial distances from the center of the box. At low spatial separations (typically up to  $\sim 1$  kpc), the power law index of the VSFs is likely dominated by effects of numerical viscosity, leading to artificially increasing power law indices (see also Grete et al. 2023b, for a more extensive discussion on this effect). At larger separations,

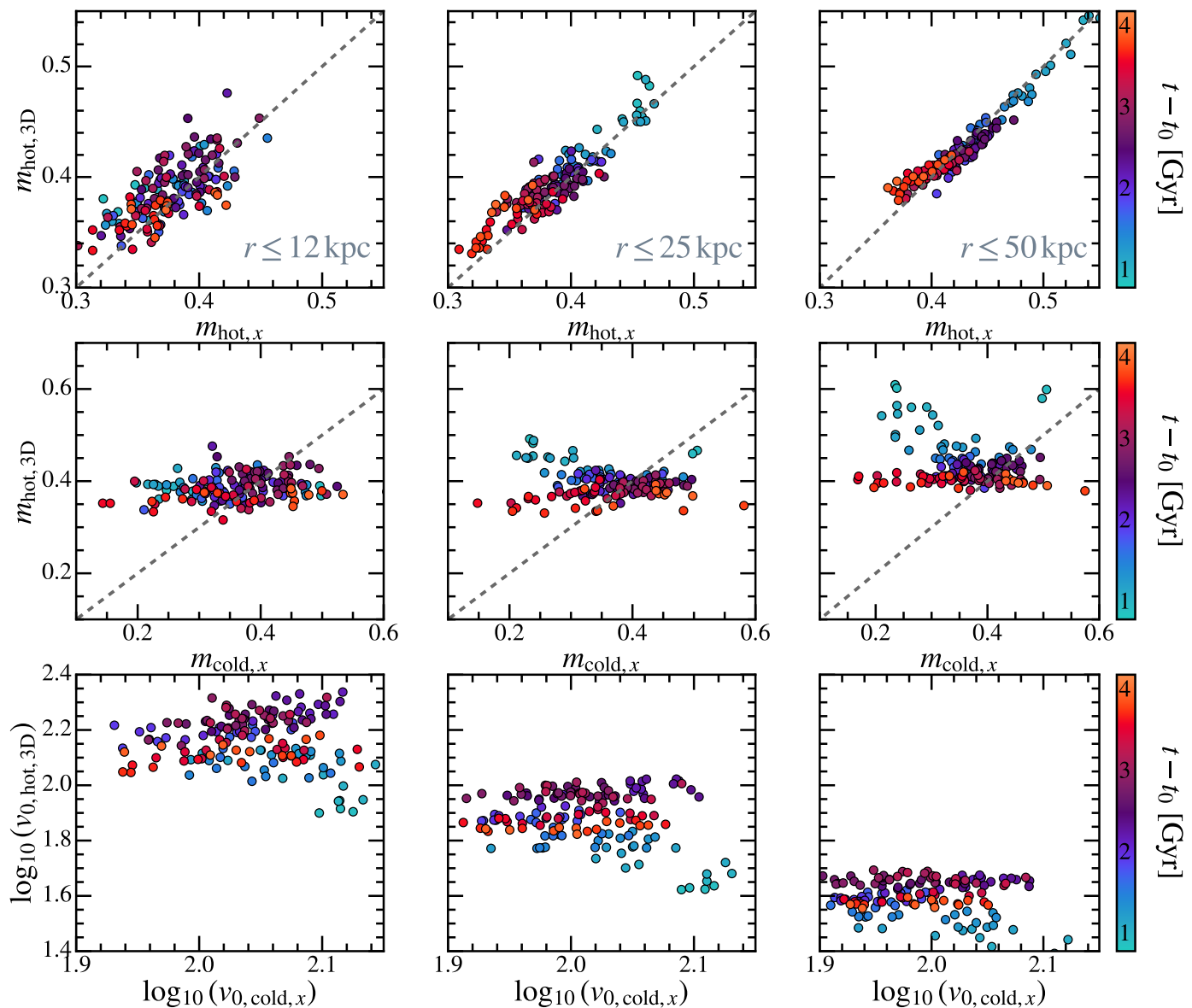


**Fig. 5.** Top panels: relationship between the power law index of the line-of-sight hot gas VSF and that of its three-dimensional counterpart. Middle (bottom) panels: relationship between the power law index  $m$  (amplitude  $v_0$ ) of the line-of-sight, cold phase VSF and the three-dimensional hot phase VSF respectively. The color of the points represents time, with values ranging from 0.9 to 4.0 Gyr. The columns show VSF values for all gas within radii of 12, 25, and 50 kpc (left to right). The dashed gray line indicates the identity relationship and should not be interpreted as an attempt to fit the data. The light blue shaded area represents the region of the parameter space where the measured power law index of the VSF is steeper than the  $m = 1/3$  power law index predicted by the Kolmogorov theory.

both the time-averaged three-dimensional and line-of-sight VSFs are steeper than the Kolmogorov scaling. There is no significant variations of this scaling when including gas at larger radii. The cold phase VSFs follow a power law with a constant index between  $\sim 500$  pc and  $\sim 10$  kpc. The time-averaged VSFs are typically steeper than the Kolmogorov scaling index of  $m = 1/3$ , and of the order of  $m \sim 0.4$ . In both phases, only including the  $x$ -component of the velocity vector decreases the amplitude of the VSFs by a factor of  $\sim 2 - 3$ , which is larger than the  $\sqrt{3}$  ratio expected in the case of isotropic turbulence.

Several previous studies have discussed the possibility of using  $H\alpha$ -emitting gas or surface brightness fluctuations of the X-ray luminosity as a proxy to trace the hot gas VSF. In Fig. 5, we present the relationship between the power law index of the line-

of-sight ( $m_{\text{hot},x}$ ) and unprojected ( $m_{\text{hot},3D}$ ) hot phase VSFs (top panels) and between that of the line-of-sight, cold phase ( $m_{\text{cold},x}$ ) and unprojected hot phase VSFs ( $m_{\text{hot},3D}$ ) (middle panels) for each snapshot. The lower panels present the relationship between the amplitude  $v_0$  of the line-of-sight, cold phase VSFs and the unprojected hot phase VSF. The left, center and right panels indicate results for VSFs obtained from all gas cells contained within a limit radius of 12, 25 and 50 kpc, respectively. Each power law index  $m$  and amplitude  $v_0$  were measured by fitting the VSFs between 2 and 4 kpc using:

$$\log_{10} S_1(\ell) = \log_{10}(v_0) + m \log_{10}(\ell), \quad (4)$$

where  $\ell$  is the separation scale and  $v_0$  is defined as the VSF amplitude. The gray dashed line indicates the identity relationship.

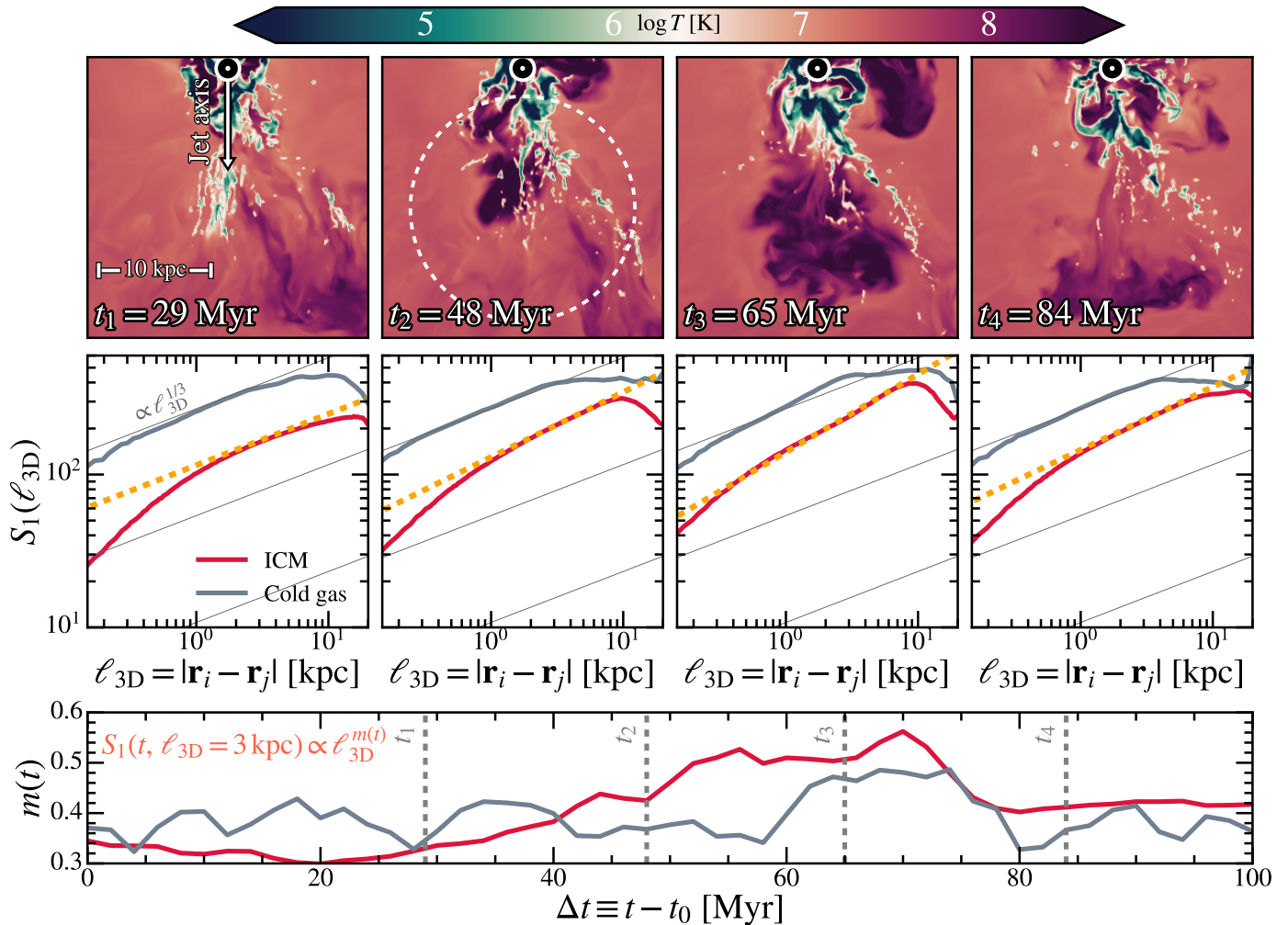


**Fig. 6.** Top panels: 1 kpc – thick temperature projection of the gas. The dashed circle indicates the sphere within which the VSF are computed. The round marker at the top of the temperature projection indicates the position of the SMBH particle and the arrow shows the jet injection axis. Middle panels: VSF of the cold (gray curves) and hot (red curves) phases. The dashed orange lines indicate the fit of the power law index of the hot phase VSF. Lower panel: time evolution of the cold and hot phases power law index.  $t_0$  here refers to the restarting time of the simulation.

While the power law index of the line-of-sight, hot gas VSF shows a good correlation with its three-dimensional counterpart, there is no visible correlation between the power law index of the line-of-sight, cold gas VSFs and that of the three-dimensional hot gas VSFs. The power law index of the hot phase VSF is relatively constant throughout the whole duration of the simulation, and is mostly centered around  $m \sim 0.4$ , with no significant variation when including gas at larger radii (see middle and right columns). The power law index of the cold phase shows more fluctuations, ranging from  $m \sim 0.2$  to  $m \sim 0.5$ . The power law index of the hot phase VSFs are preferentially steeper than their unprojected hot phase counterparts. Similarly, we find no clear correlation between the amplitude of the cold and hot phases VSFs.

### 3.3.2. Effect of rising cavities

In Li et al. (2020) and Ganguly et al. (2023), it has been suggested that features observed in the line-of-sight H $\alpha$  emitting gas VSF could be related to the presence and size of the rising cavities related to the AGN activity. In the previous subsection, we have reported the absence of strong correlation between the parameters of the VSFs for the gas located in the inner tens to

hundred of kpc of the simulated box. To evaluate the possibility that the AGN activity still might affect the VSF locally, we re-run our cluster setup simulation and save a larger number of snapshots, with an output saving interval of  $\Delta t_{\text{snap}} = 2$  Myr, starting from  $t = 1.5$  Gyr.

In Fig. 6, we present the evolution of the three-dimensional hot phase VSF evaluated in a sphere of radius  $r_{\text{sphere}} = 10$  kpc between  $t_i = 1.4$  Gyr and  $t_f = t_i + 100$  Myr. During this time, AGN activity leads to the formation of a pair of rising bubbles. To study the effect of these bubbles on the ICM kinematics, we manually position the sphere so that it encapsulates the lower (ie. in the  $z \leq 0$  half of the box) when it detach from the injection region, around  $t_3 = 65$  Myr (see temperature projection in the second and third columns). The upper panels of Fig. 6 show projections of the temperature field with a thickness of 1 kpc. The second row shows the corresponding VSFs of the hot (red curves) and cold (gray curves) phases, computed within that sphere. The thin solid gray lines indicate the Kolmogorov scaling law of index  $m = 1/3$ , while the dashed orange line indicates the fit of the hot phase VSFs. In the lower panel, we present the time evolution of the corresponding power law index for the cold and hot phases. Before the cavity starts forming, the power law

index of the VSF is around  $m = 0.3$ . As the jets inflate the cavity, the power law index of the VSF becomes steeper and increases by a factor of  $\sim 2$  to reach  $\sim 0.5 - 0.6$ . At later times, the cavity rises through the ICM, loses its spherical shape, and exits the sphere of cells under consideration. The power law index of the VSF decreases again and converges to  $m = 0.4$ . The VSFs of the cold phase show wider variations and no definitive conclusion can reasonably be drawn from the time evolution of its power law index. A peak in the VSF at scales of  $\sim 10$  kpc is visible during the phase when the cavity structure is clearly visible.

## 4. Effects of projection and comparison to observations

### 4.1. Mock $H\alpha$ observations

Current measurements of the VSF of  $H\alpha$ -emitting gas is obtained from line-of-sight measurements performed with ground-based instruments. In Li et al. (2020) and Ganguly et al. (2023), the optical imaging Fourier transform spectrometer (SITELE) and the Multi Unit Spectroscopic Explorer (MUSE) are used to create maps of the optical emission from the warm ionized phase of several BCGs. The amount of detail resolved in such maps is impacted by two parameters: the angular resolution, which is intrinsic to the instrument, and the atmospheric seeing. The latter is often modelled via Gaussian smoothing of the emission map. For the Perseus cluster, the angular resolution of SITELE translates into a physical width  $\delta x_{\text{pxl}} \sim 250$  pc. The atmospheric seeing induces a smoothing whose full width at half maximum (FWHM) is typically  $\sim 0.42$  kpc (Li et al. 2020). To evaluate the effects of spatial resolution and seeing, we produce mock  $H\alpha$  emission-weighted line-of-sight velocity maps of our simulated box. We filter the gas to keep only the cold component of temperature  $T \leq 10^5$  K. The emissivity  $j_{H\alpha}$  of gas in each cell is given by:

$$j_{H\alpha} = 3 \times 10^{-26} T_4^{-0.942-0.031 \ln(T_4)} n_e n(H^+) \text{ erg cm}^3 \text{ s}^{-1} \text{ sr}^{-1}, \quad (5)$$

where  $T_4 = T/10^4$  K and  $T$ ,  $n_e$ , and  $n(H^+)$  are the temperature, electron density, and ionised hydrogen density of each gas cell, respectively (Dong & Draine 2011). The line-of-sight, two-dimensional velocity maps are then obtained by projecting the  $x$ -component of the velocity field on the  $(y, z)$  plane. The VSF of the projected map is then obtained by sampling all available pairs of pixels. The separation between each pair of pixels is computed from their projected, two-dimensional distance. We also compute the VSFs obtained from smoothed projected maps to mimic the effect of atmospheric seeing. These maps are obtained by applying a Gaussian kernel to the original  $H\alpha$  map (see Fig. 1). In Sect 4.3.1, we compute VSFs out of projected velocity maps with degraded resolution. The method employed to generate these resolution-downgraded maps is described in the Appendix E.

### 4.2. Mock $X$ -ray observations

We also evaluate the impact of projection on the hot phase. To this end, we use the same method as for the optical emission. We separate the hot phase by only projecting gas whose temperature is above  $10^6$  K and below  $10^8$  K (to exclude the jets), and apply either no weighting, or a weighting modelling the scaling of Bremsstrahlung emission, i.e., with emissivity  $j_B \propto \rho^2 \sqrt{T}$ . A visualization of such emission-weighted projection is presented

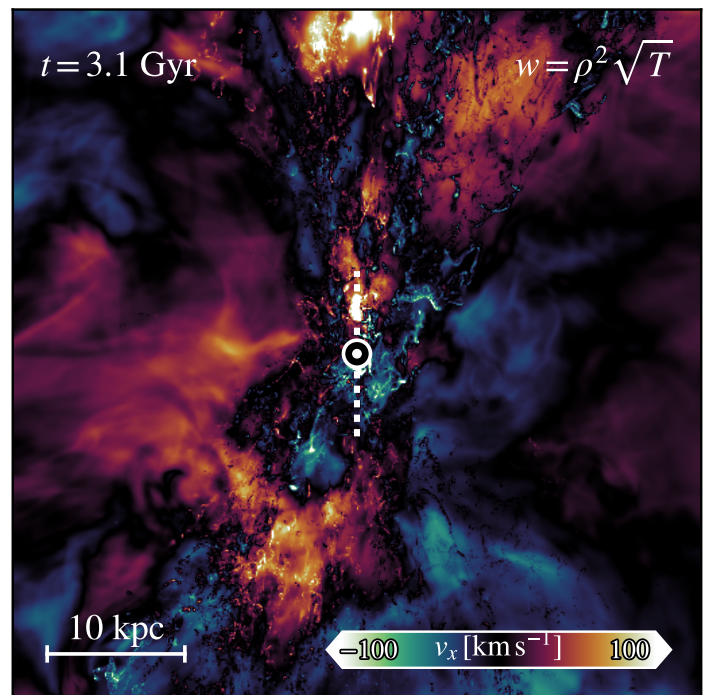


**Fig. 7.** Emission-weighted ( $w$ ) line-of-sight velocity projection of the hot phase within the inner 50 kpc of our fiducial MHD run at  $t = 3.1$  Gyr. The marker and dashed line at the center indicate the position of the SMBH particle and the axis of the jets, respectively.

in Fig. 7. Although the cold phase is filtered out from these projections, overdensities in the hot phase spatially correlated with the cold filaments are still visible.

### 4.3. Effects of projection and smoothing

#### 4.3.1. Cold phase

In Fig. 8, we show the effects of various projection methods on the resulting VSFs. All curves corresponds to the time-average of all VSFs between 0.9 and 4 Gyr for our fiducial MHD run and for all cold gas located at  $r \leq 25$  kpc. The colored areas represent the standard deviation resulting from time variation across all snapshots. The darkest curve indicates the VSF of the  $x$ -component of the velocity field, computed by taking the three-dimensional distance between each pair of cells. All the other curves are computed based on projected maps, implying that separations between pairs of pixels are computed taking their two-dimensional distances. The third curve is computed taking projected maps of the velocity field weighted by  $H\alpha$  emission. The last and brightest curve includes smoothing resulting from atmospheric seeing, assuming a smoothing kernel with a standard deviation consistent with the values expected for the Perseus cluster (i.e., a FWHM of 0.42 kpc, see Li et al. 2020). The blue vertical line indicates the full width at half maximum (FWHM) of the Gaussian kernel used to smooth the projected velocity maps. The effect of smoothing on the VSFs power law index taking other filters' kernel sizes is discussed in Appendix D.

Taking into account the three-dimensional distribution of the cold gas, the time-averaged VSF is slightly steeper than the Kolmogorov scaling law, with a mean power law index of  $m \sim 0.4$ . When calculating the VSF extracted from projected maps, the



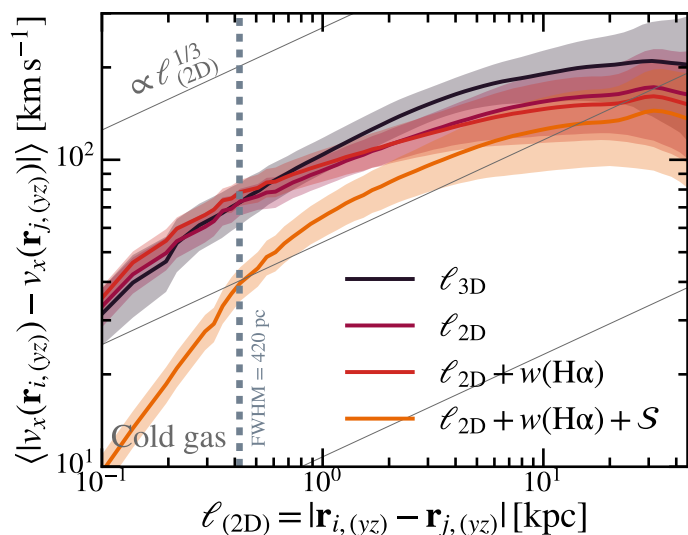


**Fig. 8.** Line-of-sight VSFs for the cold component and for projected radius  $r \leq 25$  kpc averaged between 0.9 and 4 Gyr. The darkest curve (labelled  $\ell_{3D}$ ) is obtained taking the three-dimensional distance between pairs of points, similarly to Wang et al. (2021). For all the other curves, the VSFs are computed out of projected maps, and the corresponding separations scales are two dimensional ( $\ell_{2D}$ ).  $w(\text{H}\alpha)$  indicates weighting of the map by  $\text{H}\alpha$  emission, and  $S$  the additional smoothing effect resulting from atmospheric seeing (see Li et al. (2020)). The shaded areas indicate the time variation of each VSF.

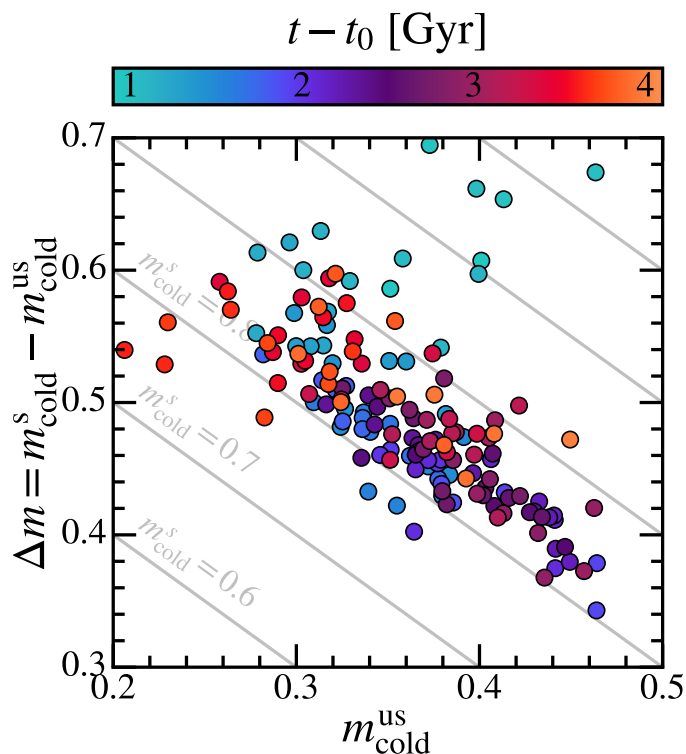


**Fig. 9.** Relationship between the power law index  $m_{\text{cold}}^{\text{us}}$  of the unsmoothed (“us”) projected VSFs (horizontal axis) and  $\Delta m$ , which represents the increase in the power law index resulting from smoothing. Lines of equal power law index for smoothed VSFs ( $m_{\text{cold}}^{\text{s}}$ ) are also indicated for comparison (grey lines).

time-averaged VSF flattens and its power law index reduces to  $m \sim 0.2$ . Including weighting by  $\text{H}\alpha$  emission has little impact

on the power law index, although leading to a minor additional flattening with respect to the unweighted projected VSF. Finally, when taking into account the effect of atmospheric seeing on our maps by applying a Gaussian smoothing kernel, the power law index of the VSF is dramatically increased. Below scales of the order of the smoothing kernel size, the power law index is close to  $m = 1$ . Above this typical scale, the effect of smoothing on the power law index becomes less significant, although it still affect the overall amplitude VSF. Since we use a smoothing kernel assuming the distance to the Perseus cluster, the expected effect of smoothing on the line-of-sight velocity maps of galaxy clusters located further away could be more important.

To evaluate the effect of smoothing on individual VSFs for scales of the order of the smoothing kernel size, we present in Fig. 9 the relationship between the power law index  $m_{\text{cold}}^{\text{us}}$  of the unsmoothed (“us”) projected VSFs (horizontal axis) and  $\Delta m$ , which represents the increase in the power law index resulting from smoothing. All power law indices are obtained by fitting the VSFs for separations of  $\ell = 0.4 \pm 0.1$  kpc. As a comparison, lines of equal smoothed VSFs power law index  $m_{\text{cold}}^{\text{s}}$  are represented with the solid grey lines. Intrinsically shallower VSFs are more affected by smoothing than the steeper ones, as  $\Delta m$  varies broadly linearly with  $m_{\text{cold}}^{\text{us}}$ , with a slope close to  $-1$ . Consequently, the power law index of the smoothed VSFs remains relatively constant across snapshots, with  $m_{\text{cold}}^{\text{s}} = 0.86 \pm 0.06$ .

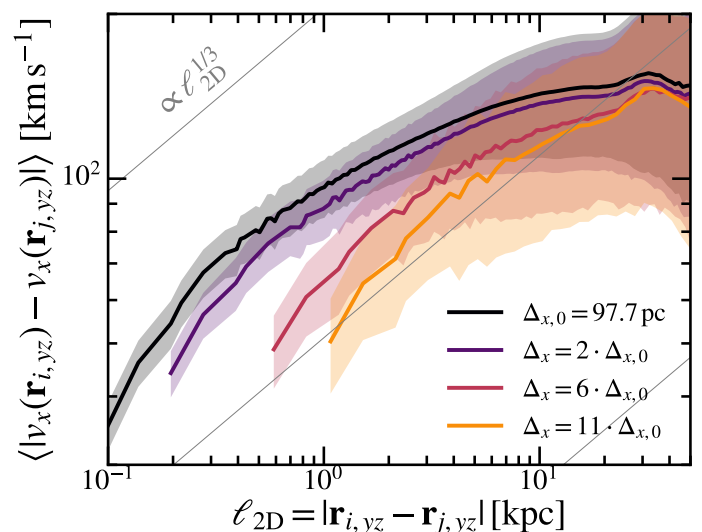


**Fig. 10.** VSFs obtained from projected maps taking various spatial resolutions for the gas located at projected radius  $r \leq 25$  kpc. The projection method for all curves is equivalent to the third curve in Fig. 8 (i.e., labelled as  $\ell_{yz} + w(\text{H}\alpha)$ ). Consequently, the VSFs presented here are shallower than their three-dimensional counterparts (labelled as  $\ell_{3D}$  in Fig. 8) due to projection and emission weighting. The darkest curve corresponds to the maximum spatial resolution  $\Delta_{x,0}$  of our simulation. All brighter curves are obtained from coarse-grained maps with pixel size  $\Delta_x$ . The colored areas represent the standard deviation resulting from time variation across all snapshots.

Instruments used to obtain line-of-sight velocity maps of galaxy clusters have limited angular resolution, translating into limited spatial resolutions depending on the distance of the observed galaxy. To evaluate possible consequences on the VSFs, we present in Fig. 10 the influence of varying spatial resolution on the velocity maps of the cold phase. While the darkest curve is

computed using projected maps with pixels of width  $\Delta_{x,0} = 97.7$  pc (corresponding to the maximum resolution of our simulation setup), all brighter curves correspond to VSF obtained from maps with degraded resolution, resulting in pixels of width  $\Delta_x = k \Delta_{x,0}$ , where  $k$  is an integer. Downgrading the resolution leads to a steepening of the VSFs. The typical VSF amplitude decreases for separations scales lower than the domain size (i.e., for  $\ell \sim 25$  kpc).

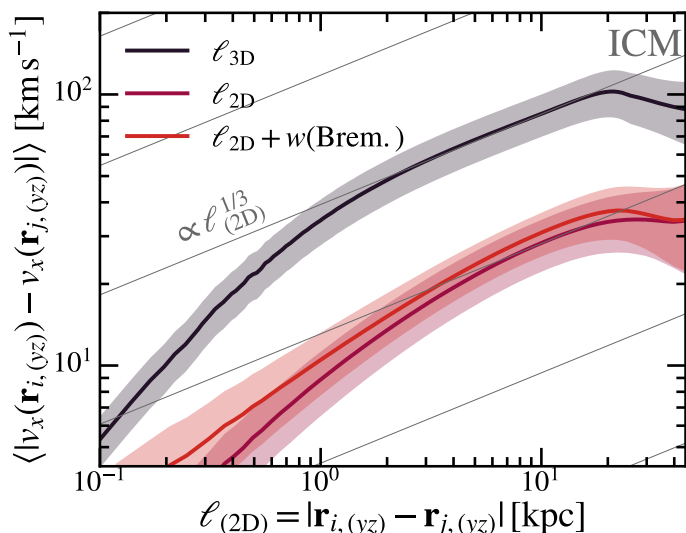


**Fig. 11.** Same as Fig. 8 for the hot phase. The brightest curve indicates the VSF obtained from Bremsstrahlung emission weighted velocity maps. The projected VSFs are steeper than the unprojected one for separations above  $\ell \sim 1$  kpc. The emission-weighted VSF becomes shallower at lower separations.

#### 4.4. Hot phase

In Fig. 11, we study the effects of projection on the VSF of the hot phase in a similar way as we did in Fig. 8 for the cold phase.  $w(\text{Brem})$  indicates that the VSFs were obtained from Bremsstrahlung emission – weighted velocity maps. The amplitudes of the projected VSFs at any scale are typically lower by a factor of  $\sim 2$  compared to the three-dimensional VSFs. Both projected VSFs (weighted and unweighted) are steeper than the three-dimensional VSF for separations above  $\ell \sim 1$  kpc, and have power law index of  $m \sim 1/2$ . Including Bremsstrahlung emission weighting makes the VSF shallower than the unweighted and unprojected ones for lower separations. This is likely resulting from the presence of overdensities in the hot phase spatially correlated with the cold phase (see Fig. 7). These results are broadly consistent with that reported from turbulent box simulations (see the projected and unprojected VSFs of the radiative MHD run `f0.10magHR` in Fig. 7 from Mohapatra et al. 2022, for a direct comparison).

#### 4.5. Effects of the observer orientation

In Fig. 12, we present a set of 2,000 VSFs computed from  $H\alpha$  emission-weighted maps of the cold gas line-of-sight velocity in the inner 50 kpc of our simulated cluster at  $t = 3.2$  Gyr. Each map is obtained by projecting the line-of-sight velocity of each cold gas cell along a randomly selected orientation identified by its azimuthal and polar angles ( $\phi, \theta$ ). As discussed

earlier, the VSF do not follow a power law with a fixed index within the whole interval of separations considered here, as numerical viscosity results in artificially steeper VSF for spatial separations of a few cells. Here, we thus fit the VSF between 2 and 4 kpc, above the region affected by numerical viscosity and below the window effect resulting from the limited domain size. Varying these boundaries does not result in major changes as the power law typically keeps a constant index between 2 and 10 kpc. The values for  $v_0$  and  $m$  are then presented following an Aitoff projection. Since we do not include effects of opacity during the projection of the velocity map, and the left and right half of the Aitoff projection are symmetrical for both  $v_0$  and  $m$ . The injection axis of the jets corresponds to  $\theta = \pm 90^\circ$ , i.e., the vertical axis at  $\phi = 0^\circ$ .

While the typical VSF amplitudes does not vary strongly along the azimuthal angle  $\phi$ , it varies of nearly a factor of two between viewing angles parallel to the the midplane of the simulated box ( $\theta = 0^\circ$ ) and those parallel to the jet axis ( $\theta = \pm 90^\circ$ ). This is likely related to the orientation of the filaments, which tend to align with the AGN jet axis. Since they are preferentially in-falling structures, their line-of-sight velocity amplitude is larger along the  $z$  axis than the perpendicular directions with respect to the jets. As roughly half of the gas is falling along the  $+z$  direction and the other half along the  $-z$  direction, this bipolarity results in larger velocity differences at separations of the order  $\ell \leq 10$  kpc. The power law index of the VSF also varies by more than a factor of 2 depending on the observer’s orientation. Its value is typically found between  $m = 0.15$  and  $m = 0.35$ , and is on average shallower than the Kolmogorov value of  $1/3$ . We attribute this flattening to projection (see Sect. 4.3).

#### 4.6. Comparison with optical observations

In order to compare our results to those in Li et al. (2020), we show in Fig. 13 time-averaged VSFs of the cold gas obtained from  $H\alpha$  emission-weighted maps. The maps have been coarse-grained to a spatial resolution of 291 pc (the actual resolution of the SITELLE instrument is approximately 255 pc, but the coarse-graining method used here only permits reducing the resolution by integer multiples of the original map’s spatial resolution, namely 97 pc). “Inner”, “outer”, and “all” (see legend) designate the VSFs obtained from all gas cells located at projected radii less than 12 kpc, at projected radii more than 12 kpc, and for all gas cells, respectively. Gray curves correspond to the VSF inferred from optical observations and are taken from Li et al. (2020). The left and right panels show results for VSFs calculated from unsmoothed and smoothed, projected velocity maps, respectively. The unsmoothed, coarse-grained map is typically shallower than the Kolmogorov scaling law  $m = 1/3$ . The amplitude at low spatial separations is also greater than observations by a factor of two. Smoothing results in time-averaged VSFs that have power law index and amplitude more consistent with observations. We note that numerical viscosity can impact the dynamics of gas for separations lower than  $\ell \sim 1$  kpc (see Sect. 5).

Time-averaging VSFs over nearly 4 Gyr (i.e., approximately 170 snapshots) naturally smoothes out many details visible in individual VSFs calculated at fixed times. Although the steepening effect due to smoothing is visible in all VSFs, the relative curvature of the time-averaged smoothed VSFs presented in the right panel of Fig. 13 does not accurately represent the typical shape of individual VSFs. To provide context for the time-averaged

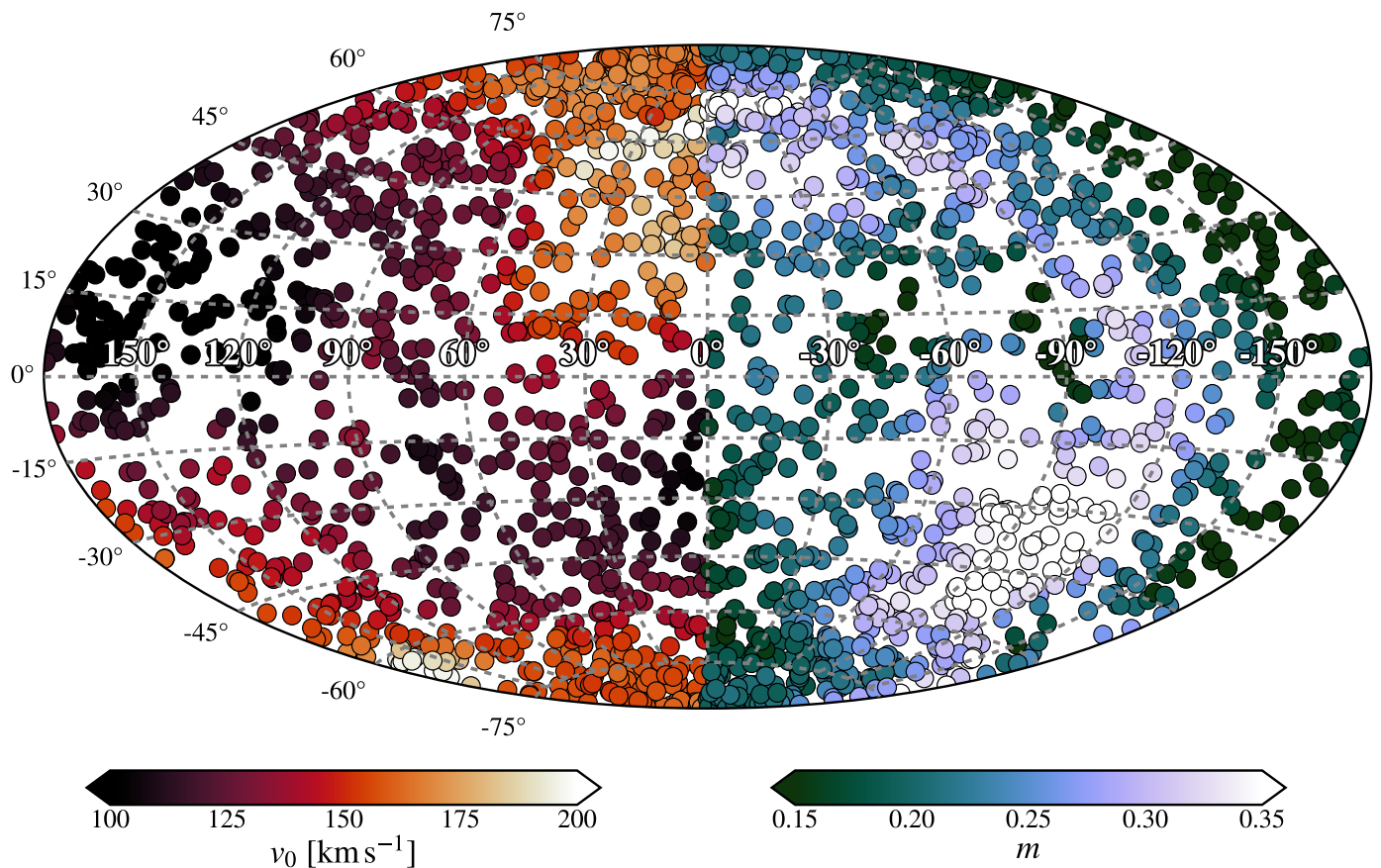


**Fig. 12.** Aitoff projection of the values of the VSF amplitude  $v_0$  and the power law index  $m$ , measured for 2,000 randomly selected orientations at fixed time  $t = 3.2$  Gyr within  $r = 25$  kpc. Each VSF is computed from projected  $H\alpha$  emission weighted maps. The power law fitting is performed between 2 and 4 kpc. As we do not include effects of opacity when generating the projection of the velocity maps used to obtain each VSF, the left and right half of the plot are symmetrical for both  $v_0$  and  $m$ . The coordinates of the jet injection axis is at  $\theta = \pm 90^\circ$ .

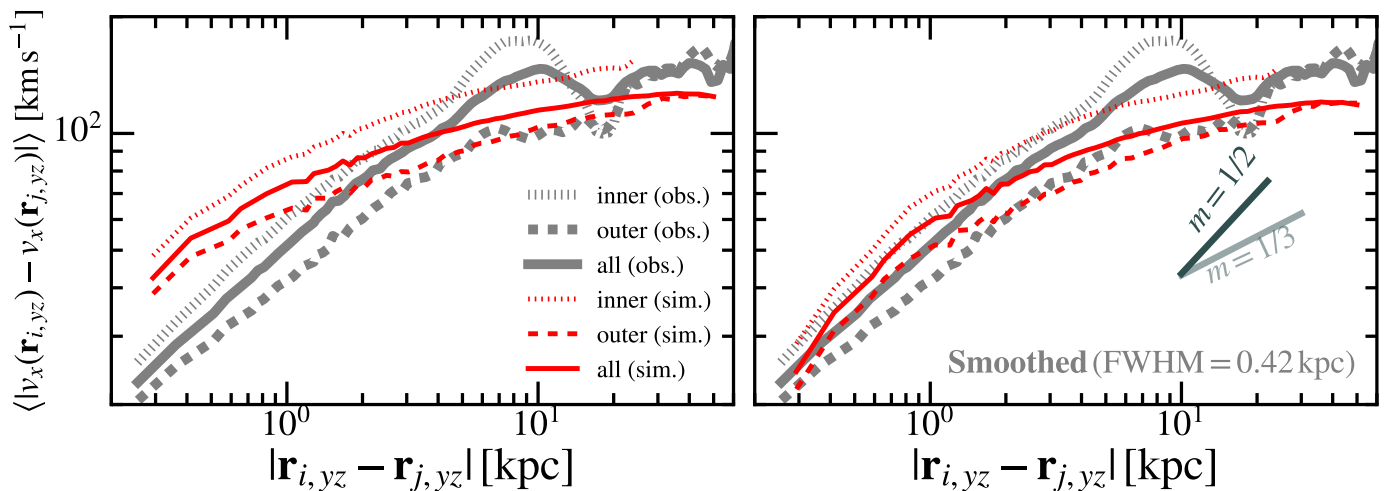


**Fig. 13.** Time-averaged VSFs of the cold phase obtained from mock  $H\alpha$  emission-weighted maps projected along the  $x$ -axis (red lines), compared to observational data (gray lines, from Li et al. 2020). The images have been coarse-grained to a spatial resolution of 290 pc to mimic the spatial resolution of instruments assuming Perseus cluster distance. The right panel is obtained from smoothed maps to mimic the effects of atmospheric seeing. inner, outer and all (see legend) designate the VSFs obtained from all gas cell located at projected radii less than 12 kpc, at projected radius more than 12 kpc and for all gas cell irrespective of their radius, respectively.

VSFs, we present in Fig. 14 individual projected and smoothed VSFs calculated at three different times, namely: 1.28, 3.28, and 3.48 Gyr. For comparison, we also include the 11 VSFs of nearby BCGs from Ganguly et al. (2023). Our individual VSFs were se-

lected to highlight typical trends observed throughout our simulation, namely: (i) VSFs characterized by a low amplitude and a relative flatness for separation scales above a few kpc ( $t = 1.28$  Gyr), (ii) VSFs exhibiting a distinct peak structure at separation

scales beyond 10 kpc ( $t = 3.28$  Gyr), and (iii) VSFs closely matching the observed VSFs both in terms of steepening and amplitude ( $t = 3.48$  Gyr). Although a visual inspection of the hot and cold phases suggests that peaks at large separations correlates with the presence and size of X-ray cavities, we were unable to rigorously establish this correlation. This is because the number of pixel pairs at separations approaching the domain size is low, leading to increased statistical uncertainty and significant scatter in the VSF values.

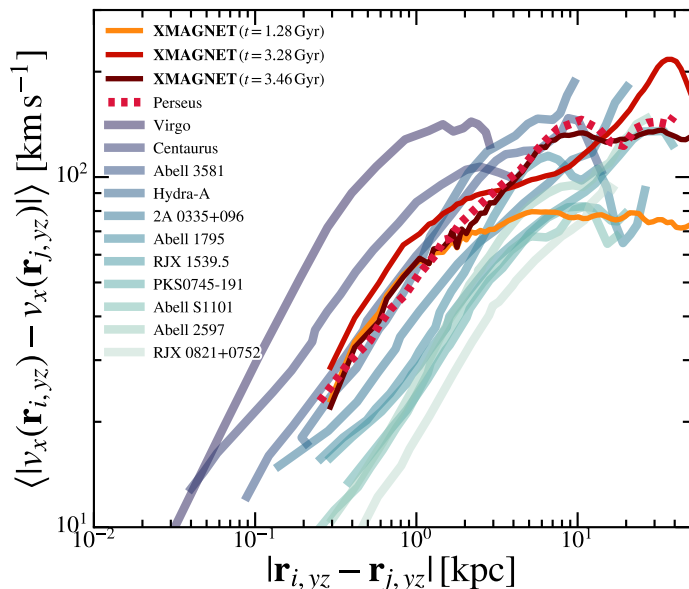


**Fig. 14.** Projected cold gas VSFs including smoothing from atmospheric seeing at three different times in the simulation: 1.28 Gyr, 3.28 Gyr, and 3.48 Gyr (orange, red and purple lines). For comparison, we also include the 11 VSFs of nearby BCGs from Ganguly et al. (2023) (thick blue lines and red dashed line).

## 5. Discussion

### 5.1. On the steepening of the velocity structure functions

Although our results suggest that smoothing from atmospheric seeing may artificially steepen VSFs, they do not rule out the possibility of an intrinsic steepening in either the cold or hot phase VSFs. As shown in Fig. 9, the impact of smoothing depends on the intrinsic power law index of the unsmoothed VSF. Since VSFs with intrinsically steeper slopes experience weaker steepening from atmospheric seeing, it is possible that VSFs measured from observations of nearby BCGs are intrinsically steeper than the Kolmogorov scaling law of  $\ell^{1/3}$ , artificially steepened by smoothing, or a combination of both.

Also, several arbitrary parameter choices in our model could significantly impact gas dynamics and, consequently, the resulting VSFs. As discussed in Sect. 2, our radiative cooling algorithm assumes a constant and homogeneous metallicity of the gas. This likely leads to an overestimation of the cooling rate at radii beyond  $\sim 25$ – $50$  kpc, which in turn may result in unrealistically extended cold gas structures and eventually excessive radial velocities. Additionally, our feedback parameters—such as jet density—could lead to a different jet-ICM coupling than seen in other simulations. For instance, Beckmann et al. (2019) demonstrated that precessing low-density jets can strongly interact with

the cold phase, producing effects not observed in our setup, such as the coherent outward motion of entire cold gas structures. However, it seems unlikely that the specific choices of our setup can alone fully explain the effects reported in, e.g., Fig. 12 and 13, which we attribute to observational limitations. The effect of smoothing on projected maps has been investigated in recent observational studies, which conclude that atmospheric seeing causes a global steepening effect on the VSFs (see notably Chen et al. 2022, and Li, McNamara, et al., submitted). The absence of magnetic fields in a purely hydrodynamical setup might also lead to steeper VSFs in the cold phase due to the preferentially disk morphologies reported in many previous studies (e.g., Li & Bryan 2014; Beckmann et al. 2019; Qiu et al. 2019; Fournier et al. 2024). A qualitative comparison between projected cold gas VSFs from the purely hydrodynamical and the fiducial MHD run of the XMAGNET suite is presented in Appendix A. We note that recent observational work focusing on jellyfish galaxies has shown that removing rotational components and large-scale motion can lead to a significant reduction in the observed steepness of the VSFs (Chen et al. 2022; Ignesti et al. 2024).

Moreover, it has been shown that numerical viscosity affects the motion of the simulated fluid (Grete et al. 2023b), and that velocity differences computed between pairs of cells located less than 8–10 cells apart (i.e., up to a physical scale of  $\sim 1$  kpc in our setup) are thus likely to be underestimated. This is likely to impact the unprojected VSFs presented in Sect. 3 since the separations between pairs of cells are computed in 3D, and we attribute the significant steepening of, e.g., the hot VSFs at separations lower than 1 kpc to this effect (see Fig. 4). Evaluating how much this might affect the projected VSFs presented in Sect. 4 is not straightforward. Each pixel of the underlying projected velocity maps corresponds to a single velocity value obtained from the averaging of up to hundreds of cells along the line-of-sight, potentially located tens of kpc away from each other. The two-dimensional distance between any given pair of pixels from a projected map is thus not indicative of the underlying three-dimensional distribution of gas cells. This may result in a dilution of the numerical viscosity, and we could expect projected VSFs to be less sensitive to this bias. This effect although remains hard to quantify and we postpone such analysis to future work.

### 5.2. Comparison to other studies

In Mohapatra et al. (2022), periodic box simulations with turbulence driving are used to study the effects of radiative cooling, magnetic fields, as well as projection and emission weighting on first and second-order VSF of the hot and cold phases of the ICM. One key result of their work is that the three-dimensional hot phase VSF is always steeper than the Kolmogorov prediction. Our analysis of the first order VSF supports such conclusions, as we find a scaling close to  $\ell^{1/2}$  near the driving scale, and even steeper at smaller scales (i.e., below  $\sim 1$  kpc). However, we find that the cold phase moves differently owing to the radial stratification in the gravitational field of the cluster. Consequently, it is less coupled to the hot phase, and dominated by a preferentially infalling motion towards the centre. A direct consequence is that we find the cold phase VSF to be always shallower than the hot phase VSF, and slightly steeper than the Kolmogorov scaling of  $\ell^{1/3}$ .

A simulation setup closer to ours is presented in Wang et al. (2021). In this work, an idealized cool-core cluster with AGN feedback, radiative cooling, and magnetic field is followed. Static grid refinement is used and the VSFs are calculated for gas located at distances less than 10 kpc away from the center of the box. The two main differences with respect to our setup are: (i) the grid structure: our maximally refined region has a width of 250 kpc versus  $\sim 20$  kpc in Wang et al. (2021), allowing us to quantify turbulence at much larger radii without refinement level transition effects or varied scales of numerical viscosity across levels, and (ii) the AGN feedback mixture: we used a three feedback channels, namely thermal, kinetic, and magnetic, while the AGN feedback is purely kinetic in Wang et al. (2021). In this work, the authors conclude that the motion of the cold filaments is mostly driven by gravitational acceleration, possibly slowed down by magnetic fields in the MHD case. The authors also find a correlation between the AGN activity and the power law index of the hot phase VSF. Quiescent periods give rise to shallower VSFs as compared to active periods. Our results are broadly consistent with the conclusions of this study. The amplitudes and scalings of our line-of-sight VSFs are close to that of their fiducial MHD run (see Fig. 4 in Wang et al. (2021) and the dashed lines in Fig. 4 of our study for a direct comparison). As reported in Grete et al. (subm.), the AGN activity in our setup does not exhibit significant duty cycles as it is mostly switched on throughout the entire duration of the simulation, with a power of  $P_{\text{AGN}} \sim 10^{45}$  erg s $^{-1}$ . Thus, we do not observe the same alternation between steeper and flatter VSFs correlated with active and quiescent phases, as shown in Fig. 7 of Wang et al. (2021). However, we find evidence that a time-dependent steepening of the VSF is present when the selection of pixel pairs is biased toward regions around rising cavities (see Fig. 6).

### 5.3. Missing physics

Our work presents a simplified and idealized modelling of a cool-core cluster. We ignore several phenomena and components which could impact our results. These include:

- The contribution of orbiting cluster galaxies and sloshing to the local turbulence in the core of the cluster: in our setup, we only model the BCG, although the motion of the other galaxies of the cluster is known to contribute to the overall level of turbulence inside the cluster (Fielding et al. 2020).
- The contribution of cosmic rays, which may affect the self-regulation of cool-core clusters (Jacob & Pfrommer 2017; Beckmann et al. 2022) and possibly the formation and morphology of cold structures (Huang et al. 2022).
- The impact of a radially-dependent metallicity profile: we consider an ICM with a constant metallicity of  $1.0 Z_{\odot}$ . While this reproduces well metallicities measured in the inner tens of kpc of cool-core clusters (Sanders & Fabian 2007; Mernier et al. 2017; McDonald et al. 2019), we might overestimate cooling at larger distances (typically at radius  $r \geq 25 - 50$  kpc), resulting in cold structures that are more elongated than measured in real cool-core clusters.
- Uncertainties on the AGN feedback parameters: many jet parameters remain largely unconstrained, such as the jet material density and temperature. Changing our jet parameters might impact the way AGN outflows propagate (e.g., Weinberger et al. 2023), and consequently the kinematics of the cold phase and the development of turbulence (e.g., Beckmann et al. 2019).

## 6. Conclusions

We have performed MHD simulations of AGN feedback in a cool-core cluster with an unprecedented combination of high resolution ( $\Delta_x = 97$  pc) and large grid size ( $2,560^3$  cells in the inner region). This simulation was run on Frontier, the first exascale supercomputer available to academic researchers (Atchley et al. 2023) and was performed with the AthenaPK code. Our setup includes gravity, radiative cooling, and a model of cold gas-triggered AGN feedback that converts accreted gas into bipolar magnetized, kinetic jets and thermal energy. The dimensions and resolution of the innermost maximally refined grid allowed us to study turbulence while minimizing numerical effects from transitions between refinement levels.

Our main conclusions can be summarised as follows:

- Quantifying the typical line-of-sight and radial velocities of the hot and cold phases, we find that the two phases have significantly different kinematic properties. The hot phase is close to hydrostatic equilibrium, with velocity dispersions lower than that measured in clusters with X-ray calorimeters by more than a factor of two. The cold phase follows a ballistic motion and is characterized by infalling and outflowing motions with velocities of up to  $\pm 10^3$  km s $^{-1}$ .
- In unprojected VSFs, we find no clear correlation between the VSF properties of the hot and cold phases. The power law index of the hot phase VSF varies only weakly over time and remains around  $m \sim 0.4$ . In contrast, the power law index of the cold-phase VSF fluctuates significantly over time, ranging from  $m \sim 0.2$  to  $m \sim 0.6$ , with a time-averaged value of  $m \sim 0.4$ .
- We find that the VSF of the hot phase around a rising cavity exhibits a transient steepening, likely related to the injection of turbulence. The power law index increases by a factor of two, reaching up to  $m = 0.6$ . This steepening lasts for a period of  $\sim 50$  Myr after which the VSF reverts to  $m = 0.4$ .
- Using mock optical images, we conclude that the cold phase VSF is significantly impacted by projection effects. Projection causes substantial flattening of the VSF, and weighting by H $\alpha$  emission further enhances this effect.
- Gaussian smoothing of the projected maps modelling the effect of atmospheric seeing significantly affects the projected VSFs at any scale. For scales below and of the order of the smoothing kernel size, the VSFs significantly steepen. Intrinsically shallower VSFs are more impacted by smoothing than steeper VSFs. For all separation scales, the amplitude of the VSFs is decreased by a factor of  $\sim 2$ .
- Changing the viewing angle leads to a variation of the amplitude and power law indices of the projected VSFs by more than a factor of 2.
- Projection effects reduce the overall amplitude of the hot-phase VSF compared to its unprojected counterpart and cause a slight steepening.

We conclude that projection effects, atmospheric seeing, and the dependence on the viewing angle must be taken into account when interpreting the VSF of the multiphase ICM. Possible extensions of this work include examining the influence of

AGN feedback parameters on the VSFs of both the hot and cold phases, exploring potential relationships between VSF features, viewing angle, and the orientation of cold filaments. Incorporating additional sources of turbulence, such as sloshing, would be also be useful to evaluate the relative contribution of the AGN induced turbulence.

*Acknowledgements.* MF thanks Ricarda Beckmann, Tirso Marin-Gilabert and Yuan Li for insightful discussions, as well as Jacob Shen for providing help with visualisation packages.

The authors thank Muzi Li and Brian McNamara for sharing a pre-publication draft of their manuscript on velocity structure functions in multiphase galaxy cluster cores.

MB and MF acknowledge funding by the Deutsche Forschungsgemeinschaft (DFG, German Research Foundation) under Germany's Excellence Strategy – EXC 2121 “Quantum Universe” – 390833306 and project number 443220636 (DFG research unit FOR 5195: “Relativistic Jets in Active Galaxies”). This research was supported in part by grant NSF PHY-2309135 to the Kavli Institute for Theoretical Physics (KITP).

BWO acknowledges support from NSF grants #1908109 and #2106575, NASA ATP grants NNX15AP39G and 80NSSC18K1105, and NASA TCAN grant 80NSSC21K1053.

This research used resources of the Oak Ridge Leadership Computing Facility at the Oak Ridge National Laboratory, which is supported by the Office of Science of the U.S. Department of Energy under Contract No. DE-AC05-00OR22725. These resources were provided by as part of the DOE INCITE Leadership Computing Program under allocation AST-146 (PI: Brian W. O’Shea).

DP is supported by the Royal Society through UKRI grant RF-ERE-210263 (PI: Freeke van de Voort).

The authors also gratefully acknowledge the Gauss Centre for Supercomputing e.V. ([www.gauss-centre.eu](http://www.gauss-centre.eu)) for funding this project by providing computing time through the John von Neumann Institute for Computing (NIC) on the GCS Supercomputer JUWELS at Jülich Supercomputing Centre (JSC).

All simulations were performed using the public MHD code *ATHENAPK*, which makes use of the *KOKKOS* (Trott et al. 2022) library and the *PARTHENON* adaptive mesh refinement framework (Grete et al. 2023a). All data analysis was performed with *yt* (Turk et al. 2011, 2024), *MATPLOTLIB* (Hunter 2007), *NUMPY* (Harris et al. 2020), *SEABORN* (Waskom 2021) and *CMASHER* (van der Velden 2020). We thank their authors for making these software and packages publicly available.

## References

Angelinelli, M., Vazza, F., Giocoli, C., et al. 2020, *Monthly Notices of the Royal Astronomical Society*, 495, 864–885

Atchley, S., Zimmer, C., Lange, J., et al. 2023, in *Proceedings of the International Conference for High Performance Computing, Networking, Storage and Analysis, SC ’23* (New York, NY, USA: Association for Computing Machinery)

Barnes, D. J., Vogelsberger, M., Pearce, F. A., et al. 2021, *MNRAS*, 506, 2533

Beckmann, R. S., Dubois, Y., Guillard, P., et al. 2019, *A&A*, 631, A60

Beckmann, R. S., Dubois, Y., Pellissier, A., et al. 2022, *A&A*, 665, A129

Biffi, V., Borgani, S., Murante, G., et al. 2016, *The Astrophysical Journal*, 827, 112

Bîrzan, L., Rafferty, D. A., McNamara, B. R., Wise, M. W., & Nulsen, P. E. J. 2004, *ApJ*, 607, 800

Brüggen, M., Scannapieco, E., & Heinz, S. 2009, *Monthly Notices of the Royal Astronomical Society*, 395, 2210–2220

Cavagnolo, K. W., Donahue, M., Voit, G. M., & Sun, M. 2009, *ApJS*, 182, 12

Chen, M. C., Chen, H.-W., Rauch, M., et al. 2022, *Monthly Notices of the Royal Astronomical Society*, 518, 2354–2372

Chiu, I., Mohr, J., McDonald, M., et al. 2015, *Monthly Notices of the Royal Astronomical Society*, 455, 258–275

Churazov, E., Vikhlinin, A., Zhuravleva, I., et al. 2012, *Monthly Notices of the Royal Astronomical Society*, 421, 1123–1135

Dolag, K., Vazza, F., Brunetti, G., & Tormen, G. 2005, *Monthly Notices of the Royal Astronomical Society*, 364, 753–772

Dong, R. & Draine, B. T. 2011, *ApJ*, 727, 35

Dunn, R. J. H., Fabian, A. C., & Taylor, G. B. 2005, *MNRAS*, 364, 1343

Ehlert, K., Weinberger, R., Pfrommer, C., & Springel, V. 2021, *MNRAS*, 503, 1327

Federrath, C., Roman-Duval, J., Klessen, R. S., Schmidt, W., & Mac Low, M. M. 2010, *A&A*, 512, A81

Felten, J. E., Gould, R. J., Stein, W. A., & Woolf, N. J. 1966, *ApJ*, 146, 955

Fielding, D. B., Tonnesen, S., DeFelippis, D., et al. 2020, *ApJ*, 903, 32

Fournier, M., Grete, P., Brüggen, M., Glines, F. W., & O’Shea, B. W. 2024, *A&A*, 691, A239

Fusco-Femiano, R. & Lapi, A. 2017, *Monthly Notices of the Royal Astronomical Society*, 475, 1340–1346

Ganguly, S., Li, Y., Olivares, V., et al. 2023, *Frontiers in Astronomy and Space Sciences*, 10, 1138613

Gatuzz, E., Sanders, J., Liu, A., et al. 2024, *A&A*, 692, A108

Grete, P., Dolence, J. C., Miller, J. M., et al. 2023a, *The International Journal of High Performance Computing Applications*, 37, 465

Grete, P., O’Shea, B. W., Glines, F. W., et al. subm. [[arXiv:2502.13213](https://arxiv.org/abs/2502.13213)]

Grete, P., O’Shea, B. W., & Beckwith, K. 2023b, *The Astrophysical Journal Letters*, 942, L34

Harris, C. R., Millman, K. J., van der Walt, S. J., et al. 2020, *Nature*, 585, 357

Hernquist, L. 1990, *ApJ*, 356, 359

Hitomi Collaboration, Aharonian, F., Akamatsu, H., et al. 2016, *Nature*, 535, 117

Hu, H., Qiu, Y., Gendron-Marsolais, M.-L., et al. 2022, *ApJ*, 929, L30

Huang, X., Jiang, Y.-f., & Davis, S. W. 2022, *ApJ*, 931, 140

Hunter, J. D. 2007, *Computing in Science and Engineering*, 9, 90

Ignesti, A., Brunetti, G., Gullieuszik, M., et al. 2024, *ApJ*, 977, 219

Jacob, S. & Pfrommer, C. 2017, *MNRAS*, 467, 1478

Kolmogorov, A. 1941, *Akademiia Nauk SSSR Doklady*, 30, 301

Lau, E. T., Nagai, D., & Nelson, K. 2013, *ApJ*, 777, 151

Li, Y. & Bryan, G. L. 2014, *ApJ*, 789, 153

Li, Y., Gendron-Marsolais, M.-L., Zhuravleva, I., et al. 2020, *ApJ*, 889, L1

Markevitch, M. & Vikhlinin, A. 2007, *Phys. Rep.*, 443, 1

McCourt, M., Sharma, P., Quataert, E., & Parrish, I. J. 2012, *MNRAS*, 419, 3319

McDonald, M., Allen, S. W., Hlavacek-Larrondo, J., et al. 2019, *ApJ*, 870, 85

Mernier, F., de Plaa, J., Kaastra, J. S., et al. 2017, *Astronomy & Astrophysics*, 603, A80

Mitchell, R. J., Culhane, J. L., Davison, P. J. N., & Ives, J. C. 1976, *MNRAS*, 175, 29P

Miyoshi, T. & Kusano, K. 2005, *Journal of Computational Physics*, 208, 315

Mohapatra, R., Jetti, M., Sharma, P., & Federrath, C. 2022, *MNRAS*, 510, 2327

Navarro, J. F., Frenk, C. S., & White, S. D. M. 1997, *ApJ*, 490, 493

Olivares, V., Salome, P., Combes, F., et al. 2019, *A&A*, 631, A22

Prunier, M., Hlavacek-Larrondo, J., Pillepich, A., Lehle, K., & Nelson, D. 2024, X-ray cavities in TNG-Cluster: AGN phenomena in the full cosmological context

Qiu, Y., Bogdanović, T., Li, Y., Park, K., & Wise, J. H. 2019, *ApJ*, 877, 47

Rasia, E., Ettori, S., Moscardini, L., et al. 2006, *MNRAS*, 369, 2013

Sanders, J. S. & Fabian, A. C. 2007, *Monthly Notices of the Royal Astronomical Society*, 381, 1381–1399

Sarazin, C. L. 1986, *Reviews of Modern Physics*, 58, 1

Scannapieco, E. & Brügggen, M. 2008, *The Astrophysical Journal*, 686, 927–947

Schure, K. M., Kosenko, D., Kaastra, J. S., Keppens, R., & Vink, J. 2009, *A&A*, 508, 751

Serlemitsos, P. J., Smith, B. W., Boldt, E. A., Holt, S. S., & Swank, J. H. 1977, *ApJ*, 211, L63

Sotira, S., Vazza, F., & Brighenti, F. 2024, *arXiv e-prints*, [arXiv:2410.07314](https://arxiv.org/abs/2410.07314)

Stone, J. M., Tomida, K., White, C. J., & Felker, K. G. 2020, *ApJS*, 249, 4

Townsend, R. H. D. 2009, *The Astrophysical Journal Supplement Series*, 181, 391–397

Trott, C. R., Lebrun-Grandié, D., Arndt, D., et al. 2022, *IEEE Transactions on Parallel and Distributed Systems*, 33, 805

Turk, M. J., Smith, B. D., Oishi, J. S., et al. 2011, *The Astrophysical Journal Supplement Series*, 192, 9

Turk, M. J., Smith, B. D., Oishi, J. S., et al. 2024, *Introducing yt 4.0: Analysis and Visualization of Volumetric Data*, <https://yt-project.github.io/yt-4.0-paper/>

van der Velden, E. 2020, *Journal of Open Source Software*, 5, 2004

Vazza, F., Brunetti, G., Gheller, C., Brunino, R., & Brüggen, M. 2011, *A&A*, 529, A17

Wang, C., Ruszkowski, M., Pfrommer, C., Oh, S. P., & Yang, H. Y. K. 2021, *MNRAS*, 504, 898

Waskom, M. L. 2021, *Journal of Open Source Software*, 6, 3021

Weinberger, R., Su, K.-Y., Ehlert, K., et al. 2023, *MNRAS*, 523, 1104

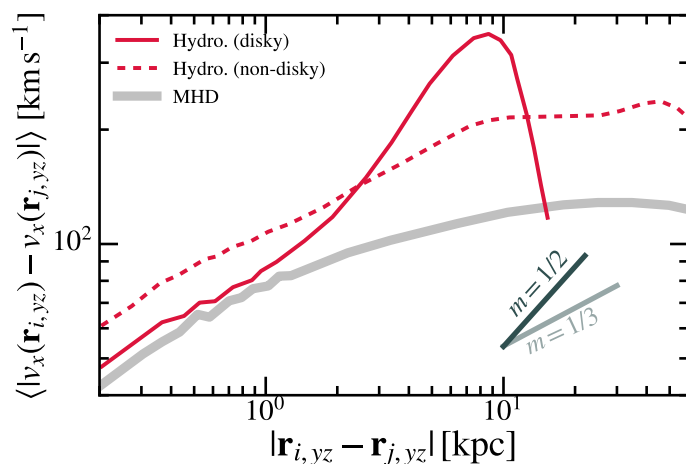
XRISM Collaboration. 2025, *arXiv e-prints*, [arXiv:2501.05514](https://arxiv.org/abs/2501.05514)

Zhuravleva, I., Churazov, E., Schekochihin, A. A., et al. 2014, *Nature*, 515, 85

ZuHone, J. A., Markevitch, M., Brunetti, G., & Giacintucci, S. 2013, *ApJ*, 762, 78

ZuHone, J. A., Markevitch, M., & Zhuravleva, I. 2016, *ApJ*, 817, 110

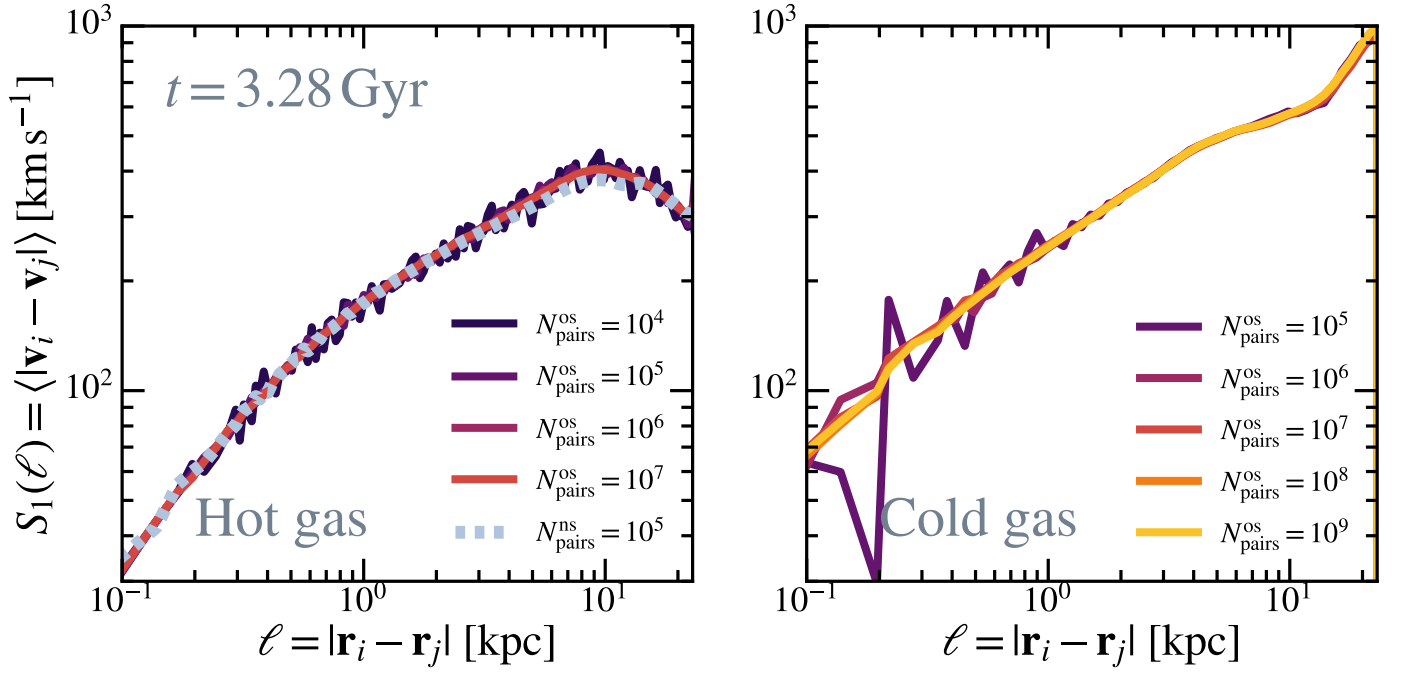
## Appendix A: Comparison with hydrodynamical setup



**Fig. A.1.** Comparison between the time-averaged projected VSFs of our hydrodynamical (red lines) and MHD (gray line) runs. In the hydrodynamical run, the gas is nearly entirely contained in a disk of radius  $r_{\text{disk}} \sim 5 - 10$  kpc for times  $t \leq 2.7$  Gyr. We thus distinguish this specific phase (solid line) from the remaining part of the run (dashed line) where no disk is visible (i.e., for  $t \geq 2.7$  Gyr).

For brevity, the results section of this paper does not discuss VSFs calculated from the purely hydrodynamical run of the XMAGNET suite. However, it is worth noting that because the structure of the cold phase differs significantly depending on the presence or absence of magnetic fields (see Grete et al. *subm.*), the resulting VSFs are also markedly different. In Fig. A.1, we present the time-averaged projected VSFs of the cold gas for our hydrodynamical (red curves) and MHD (gray curve) runs. In the hydrodynamical case, the cold gas resides in a massive disk with a radius of  $r_{\text{disk}} \sim 5 - 10$  kpc, which persists until  $t \sim 2.7$  Gyr. After this time, the disk disappears as thousands of cold clumps condense along the jet axis, increasing the total mass of cold gas in the simulation by nearly two orders of magnitude, up to  $\sim 10^{11} M_{\odot}$  (see Fig. 3 in Grete et al. *subm.*). The later phase is characterized by ballistic motion closer to what observed in the fiducial MHD run. We distinguish these two phases using two time-averaged VSFs, with the solid line corresponding to the disk phase and the dashed line to the non-disky phase.

Because the disk is rotating along an axis broadly aligned with the  $z$ -axis of the simulation's coordinate system, orthogonal to the projection axis, the resulting projected velocity maps exhibit a distinct pattern where half of the disk has positive line-of-sight velocities and the other half has negative line-of-sight velocities. This results in a characterized peak in the VSFs, visible in the solid line at separation scales broadly consistent with the disk's size (i.e.,  $r_{\text{disk}} \sim 5 - 10$  kpc). The time-averaged VSF at later times (i.e., when no disk is visible) does not exhibit any peak. Its scaling is broadly consistent with that of the MHD run (gray curve), although its mean amplitude is larger by a factor of  $\sim 2$ .

**Appendix B: VSF algorithm convergence**


**Fig. B.1.** Convergence of the VSF algorithm taking various number of pairs of cells for both the hot (left panel) or cold (right panel) phases and for the gas located at radii  $r \leq 12$  kpc at  $t = 3.28$  Gyr. “os” and “ns” designate the optimized and naive sampling methods.

Figure B.1 presents the three-dimensional VSFs of the hot and cold phases at  $t = 3.28$  Gyr, considering all gas particles within a radius of 12 kpc. For the hot phase, we compare the VSF obtained using a naive sampling method—where all cell pairs are randomly sampled—with our optimized approach, which prioritizes alternative sampling for separations below 500 pc (as detailed in Sect. 2.2). As visible, the two methods are in good agreement. We find that VSF convergence is achieved with  $10^7$  cell pairs for the hot phase and  $10^8$  for the cold phase. However, the volume filling fraction of the cold phase varies significantly throughout the simulation, particularly within the inner 12 kpc, making the number of pairs required for convergence time-dependent. This number also changes with the selected domain size. After testing convergence across multiple snapshots, we adopt  $10^7$  ( $10^8$ ) pairs for the hot (cold) phase when analyzing an  $r < 12$  kpc region. For larger domains ( $r < 25$  or  $r < 50$  kpc), we use  $10^8$  ( $10^9$ ) pairs for the hot (cold) phase, respectively.



### Appendix C: Comparison with second order VSFs

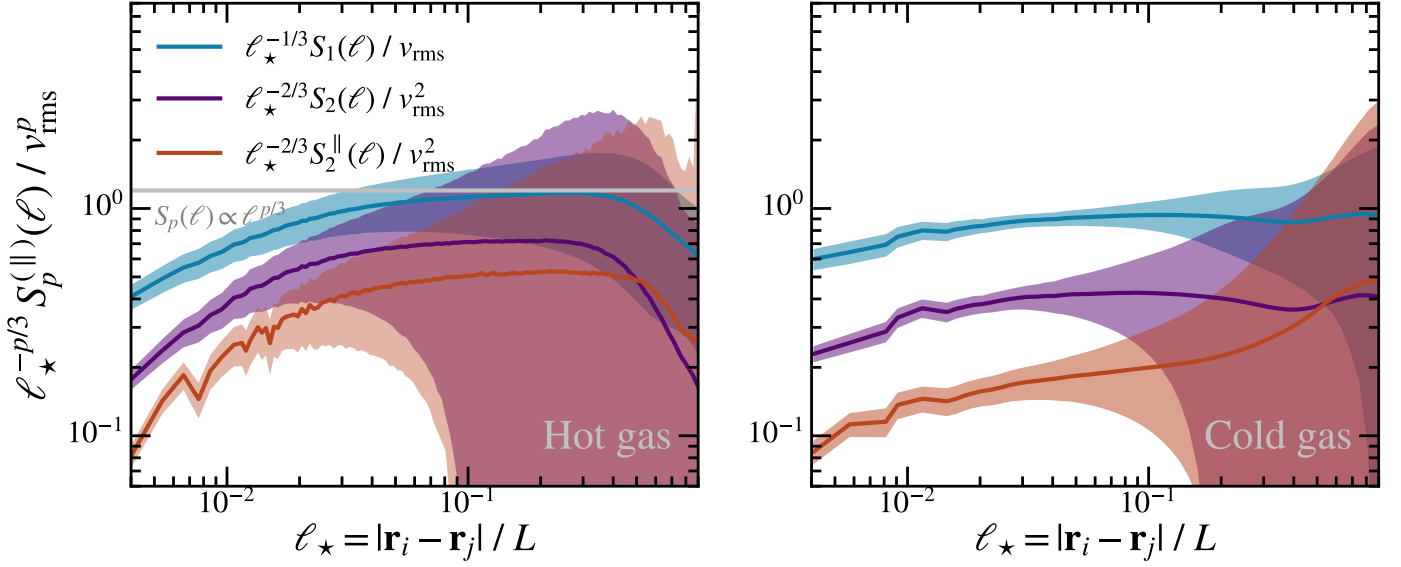


**Fig. C.1.** Comparison of the time-averaged first order VSF (blue curve), second order VSF (purple curve) and second order longitudinal VSF (red curve) for the hot phase (left panel) and the cold phase (right panel). The separations scales are normalized by the domain size  $L$  and the VSFs are normalized by their time-averaged root mean square velocity  $v_{\text{rms}}$ . The colored areas represent the standard deviation resulting from time variation across all snapshots.

In Fig. C.1, we present a comparison between the first order (blue curve) and second order (purple) VSFs for the hot (left panel) and cold (right panel) phases, calculated for the gas cells within  $r \leq 12$  kpc. All curves have been rescaled such that a  $p$ th-order VSF following Kolmogorov scaling, ie. with a power law index  $m = p/3$ , appears as a horizontal line in the plot. The Kolmogorov theory of turbulence states that  $S_2(\ell)$  and the longitudinal VSF  $S_2^{\parallel}(\ell)$  should scale similarly. For comparison we thus also present the time-averaged second order longitudinal VSF (red curve), defined as:

$$S_2^{\parallel}(\ell) = \langle \{ \mathbf{v}(\mathbf{r}_j + \ell \cdot \mathbf{e}) - \mathbf{v}(\mathbf{r}_j) \} \cdot \mathbf{e} \rangle, \quad (\text{C.1})$$

where  $\mathbf{e}$  is the unit vector pointing from cell  $j$  to cell  $i$ . The scaling of the first and second order VSFs are in good agreement.

**Appendix D: Projection depth and smoothing**

a function of the smoothing kernel size. For smoothing lengths larger than 4 pixels, the power law index converges to  $m \sim 1$ .

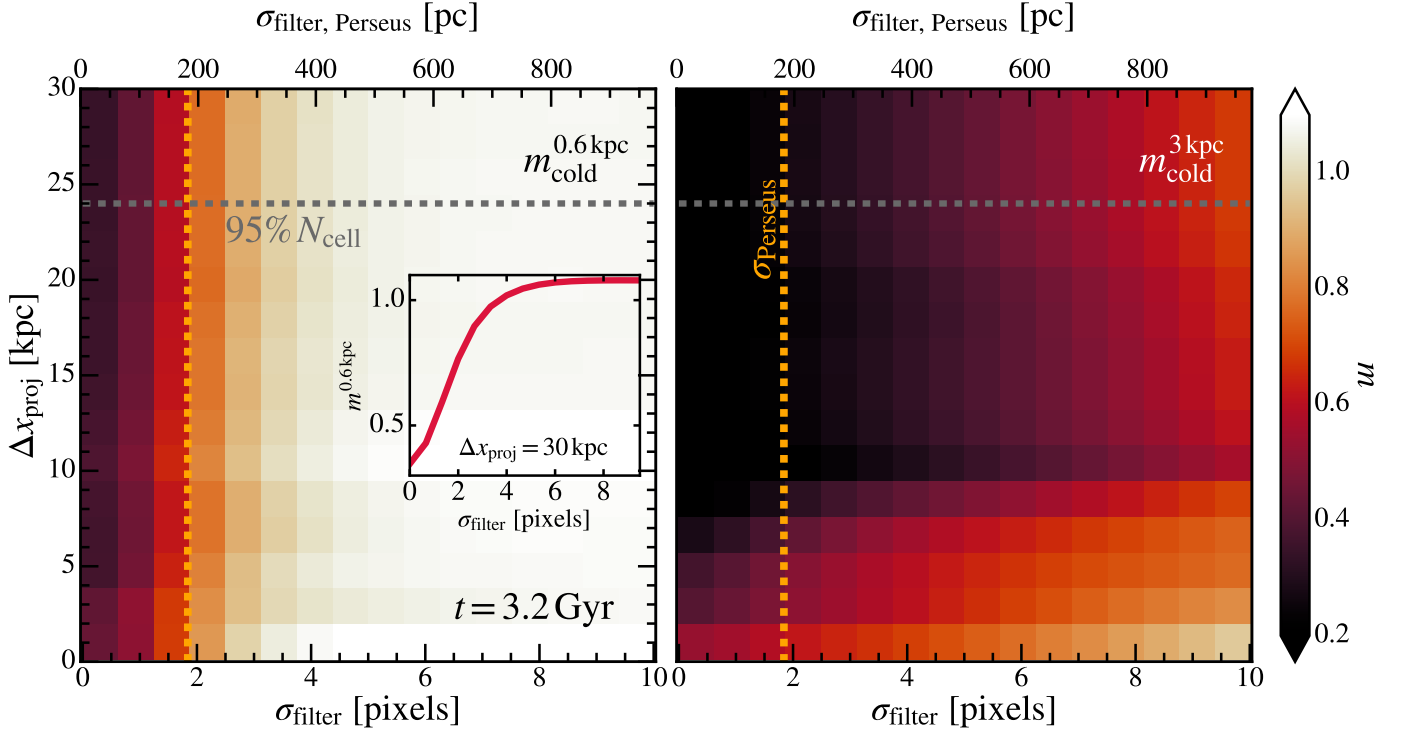


**Fig. D.1.** Various power law index measured by fitting the VSFs over  $\ell = 0.6 \pm 0.1$  kpc (left panel) and  $\ell = 3 \pm 1$  kpc (right panel) as a function of the Gaussian smoothing kernel size (expressed in pixels in the lower axis and in physical length for the upper axis, assuming the distance to the Perseus cluster for the later) on the horizontal axis and the depth of projection  $\Delta x_{\text{proj}}$  along the vertical axis. The vertical orange dashed line indicates the standard deviation  $\sigma_{\text{Perseus}}$  of the smoothing effect for the Perseus cluster. The inner figure within the left panel is a 1D visualization of the uppermost row.

In Fig. D.1, we present the power law index of VSFs measured at separation scales of 600 pc (left panel) and 3 kpc (right panel), as a function of the projection depth and smoothing length. Each pixel in the figure represents the power law index of a VSF computed from a projected velocity map. The projection is smoothed using a 2D Gaussian filter with a standard deviation  $\sigma_{\text{filter}}$ . The velocity maps include all cold gas cells within a projection depth  $\Delta x_{\text{proj}}$ , defined by the condition  $-\Delta x_{\text{proj}}/2 \leq x \leq \Delta x_{\text{proj}}/2$ , where  $x$  is the coordinate along the line-of-sight (with the SMBH particle being located at  $x_{\text{SMBH}} = 0.0$ ). The horizontal gray dashed line indicates the minimum depth of projection beyond which at least 95 % of all the gas cells contained in the simulated box are included in the projection.

As the projection depth increases more cold structures are included in the projection, modifying the power law index of the VSFs. This effect is particularly visible in the right panel, i.e., for the power law index measured at 3 kpc. The power law index measured at 600 pc, the effect of the smoothing is nearly independent of the projection depth, and more significant than at 3 kpc. A smoothing length of 2–3 pixels results in a doubling of the VSFs’ power law index. The inner figure in the left panel is a 1D visualization of the top row (including all cold gas cells of the box), showing the evolution of the VSFs’ power law as

## Appendix E: Coarse-grained velocity maps

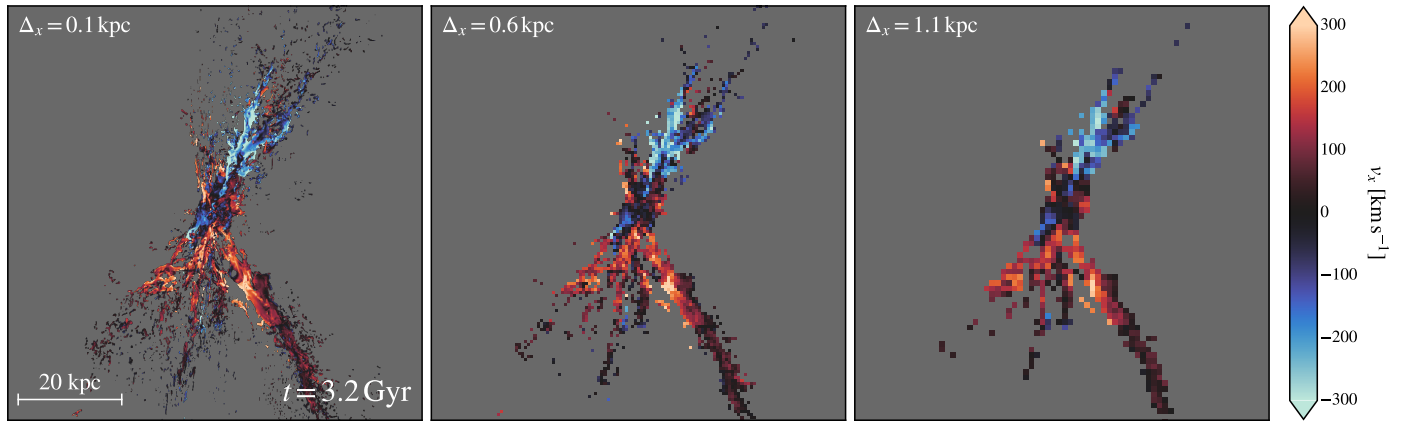


**Fig. E.1.** Comparison of three projected line-of-sight velocity maps of the same snapshot and with the same orientation. The panels indicate from left to right maps with pixel widths of 0.1 kpc (the maximum resolution of our simulation), 0.6 kpc and 1.1 kpc.

In Sect. 4.3.1, we compute the VSF extracted from projected velocity maps with degraded resolution. In order to degrade the resolution of the velocity maps, we employ a downsampling technique where the maps are coarsened by a factor  $N$ . Specifically, we group adjacent pixels into  $N \times N$  blocks, compute the mean velocity for each block, and assign the result to a single pixel in the downsampled map. During this process, we ensure that blocks with too many empty pixels (i.e., pixels corresponding to the projection of a column containing no cold gas cell) are excluded from the mean computation by applying a threshold  $s = 0.5$  on the proportion of non-empty pixels per block. A comparison of the resulting maps is presented in Fig. E.1. This threshold method allows to ignore small clumps of one or a few cells, visible in the high-resolution maps but expected to be spatially unresolved in the degraded map.